Trabajo Fin de Máster
Máster Universitario en Ingeniería Industrial

Imaging Neutral Particle Analyzer Engineering Design and installation for the ASDEX Upgrade Tokamak

Autor: Javier García Domínguez

Tutor: Juan Manuel Ayllón Guerola

Dpto. Ingeniería Mecánica y Fabricación
Escuela Técnica Superior de Ingeniería
Universidad de Sevilla

Sevilla, 2023

Trabajo Fin de Máster
Máster Universitario en Ingeniería Industrial

Imaging Neutral Particle Analyzer Engineering Design and installation for the ASDEX Upgrade Tokamak

Autor:
Javier García Domínguez

Tutor:
Juan Manuel Ayllón Guerola
Profesor Ayudante Doctor Interino

Dpto. de Ingeniería Mecánica y Fabricación
Escuela Técnica Superior de Ingeniería
Universidad de Sevilla
Sevilla, 2023

Trabajo Fin de Máster: Imaging Neutral Particle Analyzer Engineering Design and installation for the ASDEX Upgrade Tokamak

Autor: Javier García Domínguez

Tutor: Juan Manuel Ayllón Guerola

El tribunal nombrado para juzgar el Proyecto arriba indicado, compuesto por los siguientes miembros:

Presidente:

Vocales:

Secretario:

Acuerdan otorgarle la calificación de:

Sevilla, 2023

El Secretario del Tribunal

A mi familia

Agradecimientos

Agradecer a mi familia por haberme hecho llegar hasta donde estoy. A Anna por ser pura bondad y la razón por la que acabe este máster. A mis amigos y a la vez compañeros de trabajo, en especial Javier H. y Jorge, por enseñarme a disfrutar de la ingeniería y de Sevilla. A Juanma por ser un magnífico mentor y tutor de este proyecto del que tanto he aprendido, a José Rueda que sin su colaboración este diagnóstico no habría podido nunca nacer y a todo el grupo Plasma Science and Fusion Technology (PSFT).

Javier García Domínguez

Sevilla, 2023

Resumen

Se instaló un Imaging Neutral Particle Analyzer (INPA) en el tokamak ASDEX Upgrade (AUG) para proporcionar mediciones simultáneas del perfil radial y la energía de la población confinada de iones rápidos. El diagnóstico INPA aprovecha las ventajas de los analizadores de partículas neutras (NPA) y los detectores de pérdida de iones rápidos (FILD) al medir los neutros producidos del intercambio de carga ionizados por una lámina de carbono ultrafina desviada en un centelleador por el campo magnético local del reactor.

El diseño de este diagnóstico se ha desarrollado bajo una serie de condicionantes como las altas restricciones espaciales y el entorno peligroso (alto nivel de radiación neutrónica y gamma), la necesidad de alta precisión en el alineamiento del sistema óptico de 6 ejes ópticos y la optimización de la placa de centelleo (emisor de señal).

Con este fin, se ha buscado un diseño modular y flexible (periscopio ajustable) con varios grados de libertad para asegurar un posicionamiento preciso en la instalación. Las tensiones electromagnéticas y térmicas inducidas se han evaluado y comparado con los límites del material del detector.

Un análisis térmico muestra que el centelleador de diagnóstico puede funcionar de manera eficiente en condiciones normales de funcionamiento. En esta contribución se presenta el diseño CAD, un análisis de elementos finitos y una comparación entre los resultados de óptica sintética y real.

Abstract

An Imaging Neutral Particle Analyzer (INPA) has been installed in the ASDEX Upgrade tokamak (AUG) to provide simultaneous measurements of the radial profile and the energy of the confined fast-ion population. The INPA diagnostic leverages the advantages of Neutral Particle Analyzers (NPA) and Fast-Ions Loss Detectors (FILD) by measuring charge exchange neutrals ionized by a ultra-thin carbon foil deflected into a scintillator by the local machine magnetic field.

The design of this diagnostic has been developed under a series of constraints as the high spatial restrictions and hazardous environment (high level of neutron and gamma radiation), the need of high precision in the alignment of the optical system with 6 optical axes and the optimization of the scintillator plate (signal emitter).

To this end, a modular and flexible (i.e., adjustable periscope) design has been pursued with several degrees of freedom to ensure precise positioning on installation. The induced electromagnetic and thermal stresses have been assessed and compared against the material limits of the detector.

A thermal analysis shows that the diagnostic scintillator can work efficiently during normal operation conditions. The CAD design, a finite element analysis and a comparison between synthetic and real optics results are presented in this contribution.

Index

TABLES INDEX

FIGURES INDEX

1 INTRODUCTION

The industrial development and the unceasing growth of the world population, 7.9 billion, require the use of enormous amounts of energy [1]. These days, energy is still scarce and dominant by the use of fossil fuels, as can be seen in Figure 1 [2], where 77% of the global energy production in 2021 is obtained from them, (gas, coal, and oil).

The growth of energy consumption will exceed during the next 50 years and the tendency for the demand will double at the end of this century [3]. For energy production, these fossil fuels are responsible for 75% of global greenhouse gas emissions and therefore, they are the main cause of global warming.

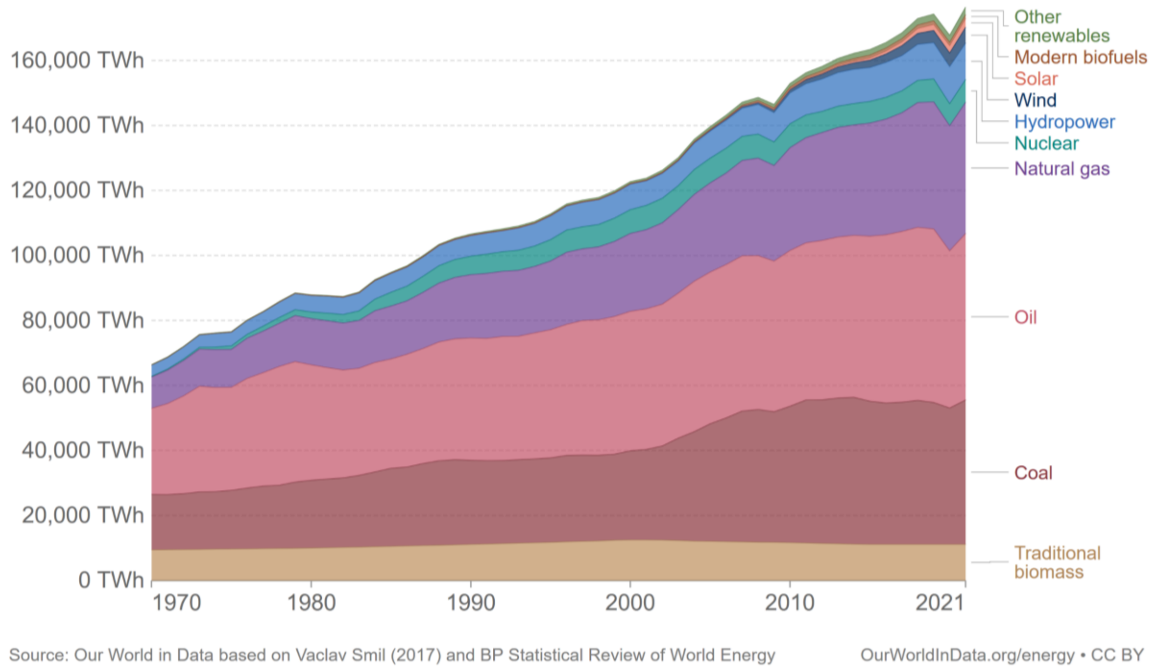

Figure 1 Energy consumption in the world, from 1970 to 2021. Reprinted from [2].

Added to this problem, the fossil fuel reserves will be spent in a range of 50-100 [4] years with the current growth demand. To overcome this difficult future situation, is essential to promote the development of clean and renewable energies capable of overcoming the use of fossil fuels over time.

Currently, the main renewable energy sources are solar, hydraulic and wind. All of them have the issues of being intermittent, very localized and limited in their storage.

Nuclear energy deals with these problems, both fusion and fission, can be prominent participants in future power generation.

Nuclear fission energy is far easier to obtain, in a technological way, compared to nuclear fusion one, and that determines that all nuclear reactor plants on earth today use fission to obtain energy.

But there are several points in fission that could make it not the best option:

- As discussed below, the energy created in a nuclear fission reaction is lower than a nuclear fusion one.
- Fuel in fission (U, Pu) is very limited and difficult to obtain.
- The long-lived radioactive waste in nuclear fission and the possibility of a nuclear accident, such as those that occurred in Chernobyl (Ukraine) or Fukushima (Japan), whose social and environmental severity in the face of a possible uncontrolled situation could limit or stop the future development of this energy.

1.1 Nuclear fusion

Nuclear fusion is the most promising energy source for the future. As an energy system generation is in research stage. Similar in benefits to nuclear fission, fusion reduces its disadvantages with much less risky nuclear wastes, because of the lower quantity produced and the short-lived products.

Fusion is naturally produced by the stars. In the Sun, hydrogen atoms fuse together to form helium, getting the particles ionized, creating a gas of charged particles called plasma. Extreme temperatures are necessary for the nuclei to overcome the electrostatic repulsive forces, Coulomb force, and get close enough to fuse them leading to the release of energy.

On Earth, the gravity interaction is lower than in the stars and the elements need to be maintained at temperatures of the order of 150 million degrees and confined for a time long enough to fuse particles.

As an atomic reaction, it generates a huge amount of energy, where the nucleus combines light atoms into a heavier one, releasing energy as the mass difference between the reactants and products following Einstein's equation $E = mc^2$. This mass transformed into energy is known as the binding energy.

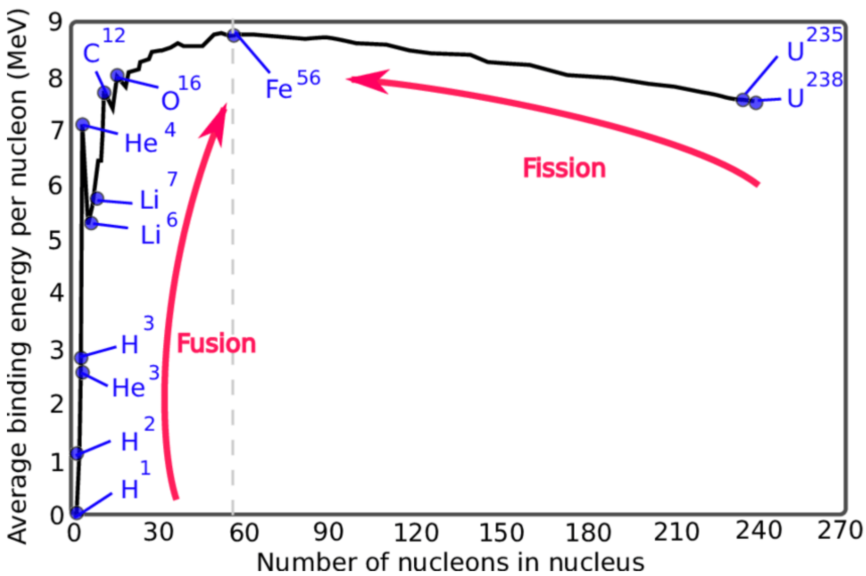

Figure 2 Binding energy per nucleon depending on the number of nucleons. Reprinted from [5].

In Figure 2 we can see the binding energy of different elements related to their atomic number. The nuclei of the heavier elements used in fission (such as U, Pu) will tend to split and the lighter ones used in fusion (such as H) will tend to fuse. When the latter merges, the dissipated bond energy is much greater than the difference between the heaviest atoms. It is estimated that nuclear fusion could reach energies 3 or 4 times higher than those of fission.

To produce a fusion reaction, the best candidates are elements (reactants) with low energy binding and fuse them creating an element (product) with a higher binding energy, that is released and used as an energy resource.

In Figure 2 shows He^4 as the best product candidate for a fusion reaction. Considering its high binding energy and a low number of nucleons in nucleus, it reduces the number of nucleons per each nucleus and so then, increases the amount of energy.

Different reactions have been proposed to achieve fusion: D-T, D-He^3, D-D, being D as deuterium (H^2), and T as tritium. Following Figure 2, the D-D rection presents itself as the best choice, as D has the lowest binding energy as a reactant for the fusion reaction. But energy is not the only parameter to consider. Figure 3 presents the cross-section parameter (probability to occur a fusion reaction) related to the kinetic energy necessary to be produced for the 3 possible reactions.

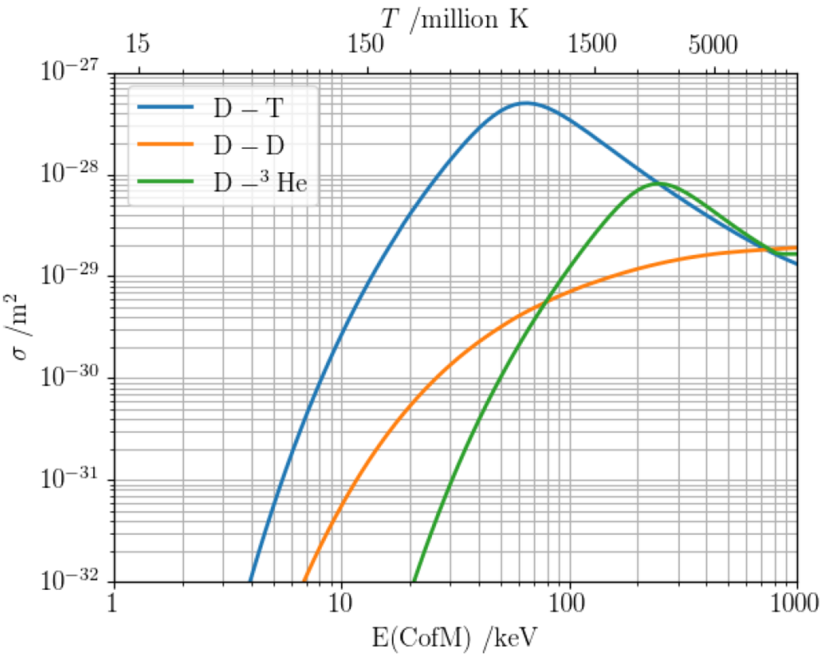

Figure 3 Cross section in a limited area (σ/m^2) vs kinetic energy (E). Reprinted from [6].

Here, in Figure 3, it is notorious why the D-T reaction is the prime candidate for the development of a commercial reactor. Different to the rest, this reaction has the highest probability of taking place with the lowest kinetic energy required.

$$D + T \rightarrow {}^4_2He(3.52\ MeV) + {}^1_0n(14.06\ MeV) \qquad (1–1)$$

Where numbers in parenthesis represent the nominal kinetic energy of the products. From this reaction, in future power plants, high-energy neutrons are produced during the reaction, which are absorbed and heated by a blanket around the core of the device. A coolant element (water, helium or Li-Pb eutectic) is passed through a blanket (the wall of the reactor) to cool it and collect the energy used to generate electricity, boiling water, producing steam for turbines and hence, generation energy.

Fusion presents the problem of developing a reactor capable of keeping the fuel in a plasma state, confined at sufficiently high temperatures and time. Once these conditions are achieved, the interactions increase, carrying out enough fusion reactions that ignition can be achieved and remain self-sustaining over time. If this event is achieved, the reactor will be able to produce more energy than is injected, generating net energy. This is the fusion energy gain factor, represented with the Q symbol. The International Thermonuclear Experiment Reactor (ITER) is currently designed to reach Q=10, from a production of 500 MW of fusion power, and a 50MW of thermal heating input power. To reach this state, Lawson's criterion needs to be fulfilled [7]:

$$n_e T_e \tau_E \geq 5.1 \cdot 10^{21} keV \cdot s \cdot m^{-3} \qquad (1–2)$$

where n_e is the electron density, T_e electron temperature, and τ_E the energy confinement time.

Nuclear fusion can get an important role in the energy market and appears as the solution to the global energy problem, if the technological development gets feasible, we can see several advantages:

- Virtually inexhaustible, without geographical impediments, cheap, stable and in great quantity.

- No emission of CO_2 or any gas that generates greenhouse effect.
- Constant and stable energy production. Net energy according to the dimensions of the reactor.
- Sustainable. Its fuels are deuterium, which can be obtained from sea water, and tritium, obtained from lithium, abundant in the earth's crust.
- No risk of collapse and no chain reaction. For the fusion of deuterium and tritium to take place, they must reach very high energies that exceed the Coulomb repulsion (repulsion of the nuclei) and form helium, so an uncontrolled chain reaction is not viable in this energy model.
- Radioactive waste is short-lived [8].

According to the European fusion roadmap, achieving a gain factor greater than one is planned for 2050, giving the opportunity to consider nuclear fusion as an important part of the energy mix in the future [9].

Last decades, fusion has taken a growing level in the scientific and social community. Getting a fusion reactor plant requires solving quite complex technological challenges and worldwide financing, similar to the major financial projects in history, such as the International Space Station or the Apollo program.

Several different approaches are chased, on Earth, to fulfill this criterion and obtain net fusion energy:

- <u>Inertial confinement:</u> Based on the compression of a fuel pellet made of tritium and deuterium and a system of really sophisticated lasers perfectly focused on the pellet. The lasers, 1 PW in 1x1 μm^2 area [10], fire against the pellet, having a high density and temperature. Despite having a very short time they can reach the Lawson criterion. This approach has reached the first Q>1, at the National Ignition Facility at Lawrence Livermore, EEUU, in 2022 [11].
- <u>Gravitational confinement:</u> Used by the stars, in consequence of their huge mass the pressure generated by gravity is extreme. Regardless of relatively low temperature, compared to the fusion required on earth, the driving factor is the density, fulfilling the Lawson criteria.
- <u>Magnetic confinement:</u> A high vacuum chamber filled by the D-T fuel in low density proportionated in state of plasma. The confinement of the plasma in an extreme temperature (150 million ºC) is essential to not to degrade the chamber. Using the fuel electromagnetic properties, with high magnetic fields, plasma particles can be guided maintaining the good behavior of the reactor. These conditions are necessary to fulfill the Lawson criterion and produce net energy.

Since this project is focused on the development of the INPA diagnostic in a magnetic confinement reactor, the rest of this text will come from this option, leaving the others out of the scope of this work.

1.2 Magnetic confinement and tokamaks

There are several approaches to create fusion from plasma confinement, such as magnetic confinement fusion and inertial confinement fusion. The most advanced is the first one, being used on this project and will be described in this section.

Deuterium and Tritium (D-T) reaction is reached in a plasmatic state. This ionized gas features electromagnetic properties and whose electrons are separated from the nuclei. Because of its extreme temperature, the plasma cannot be in contact with its container, wherewith it would be very degraded. In plasma, as the electrons escape from the nuclei, particles are ionized, therefore, reactors based on magnetic confinement use strong magnetic fields guiding particles along their field lines.

Different approaches are being developed to confine plasma by magnetic fields. The most significant machines are Tokamak and Stellarator. Both concepts are ultra-high vacuum (UHV) chambers, as the plasma container, and complex coils to create the magnetic field.

Tokamaks (*toroidal'naya kamera s magnitnymi katushkami)* were conceptualized by Russians scientists in the 50's. To the present day, tokamaks have been progressively improving, creating bigger and more powerful machines along the years, and obtaining more attention for countries in the nuclear fusion race.

Figure 4 presents the plasma magnetic confinement in a tokamak created from a set of coils:

- Toroidal Field Coils (TFC): Set of coils that wind the toroidal surface of the reactor. They generate the toroidal magnetic field.
- Central Solenoid (CS): It is the primary/secondary of a transformer. Powered with a variable electrical current, it induces a current in the plasma, secondary transformer. The plasma current induced generates a poloidal magnetic field, giving the sum between the two magnetic fields, toroidal and poloidal, resulting on a helicoidal one.
- Poloidal Field Coils (PFC): Set of coils, perpendicular to the TFC, used to control the position of the plasma generating poloidal magnetic fields.

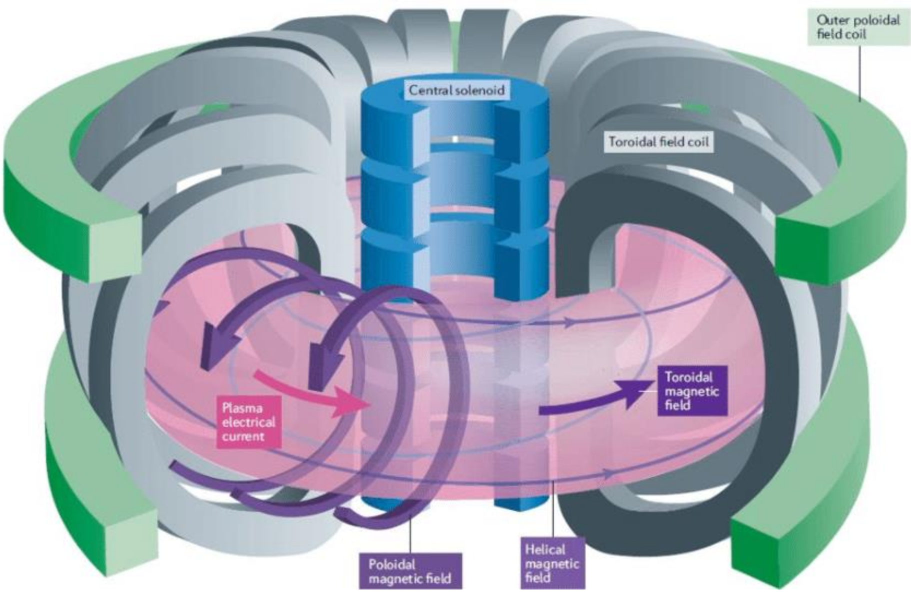

Figure 4 Illustration of the magnetic confinement in a tokamak. Reprinted from [12].

The stellarator idea is the same as the tokamak, but there are big technological differences between them. The most obvious is its shape, which is determined by the complex magnetic fields that the plasma requires to be confined. These magnetic field lines need to be helically shaped throughout the entire toroidal shape of the chamber and so then, coils, and chamber are a huge challenge from the engineer point of view. However, stellarators have the advantage of not needing to induce a current in the plasma and do not need the central solenoid. This allows them to operate in steady state, while tokamaks work in pulses. These implications are out of the scope of this work, and so then, it will not be progressed on this document.

As explained before, for a stellarator the toroidal symmetry, compared to a tokamak, is broken as the magnetic field in each poloidal plane varies. The increment of these difficulties has a strong impact on computational simulations. Tokamaks reduce coil and chamber design complexity by having an axially symmetric focus. These have been, for this reason, the main focus of the scientific community in their development, and the prior option to solve nuclear fusion with the tokamak ITER.

ITER is an international collaboration with the goal of building a tokamak producing net energy, validating the feasibility of nuclear fusion as a real energy source. ITER, as the world's largest fusion experiment, with a cost of 20 B€ [13], will have the first plasma by 2025 [14].

1.3 ASDEX Upgrade tokamak

The development of this work has been made on this machine. ASDEX (***A****xially* ***S****ymmetric* ***D****ivertor* ***Ex****periment*) tokamak was a midsize tokamak experiment in Max-Planck-Institut für Plasmaphysik, in Garching, Germany. In operation since 1980, it got renovated in 1991, renamed as ASDEX Upgrade (AUG) tokamak. Considered, from this time, the Germany's second largest fusion experiment, after stellarator Wendelstein 7-X.

The purpose of this machine is to develop the physics base for ITER and DEMO. For this reason, plasma properties, pressure, and density, are correlated to the conditions in a future fusion power plant. It is compared to other international tokamaks, as DIII-D National Fusion Facility by General Atomics in San Diego, United States of America (USA). AUG operates with D-D reaction to avoid radioactive activation of the inner surface of the chamber with D-T reaction. The purpose is to allow workers to enter the vacuum chamber without risk and increase the number of experimental improvements, during maintain periods, and transmit that information to ITER.

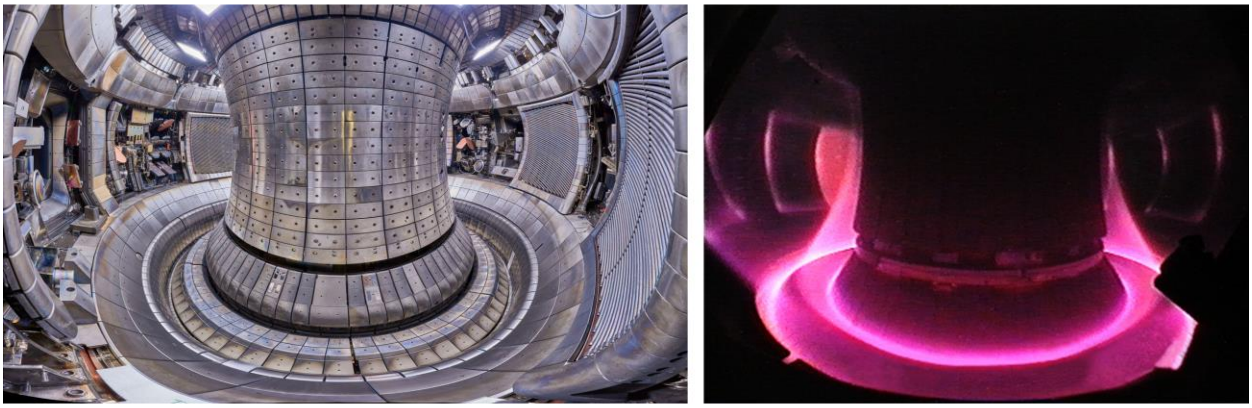

Figure 5 Images of ASDEX Upgrade in-vessel, left image during maintain periods, right image during an experiment. Reprinted from [15].

With 16 toroidal field coils and 12 poloidal field coils, it can produce a maximum total magnetic field strength of 3.2 T and a maximum plasma current Ip=1.4 MA [16]. In Figure 5 right image, is showed a pulse, where the center of the plasma is so hot that cannot be seen with conventional cameras, because its light is emitted in the non-visible spectrum. The pink light presented in the image represents the coolest plasma area.

To the ignition of the plasma is needed external heating. ASDEX Upgrade is provided with several mechanisms to external heating [17]:

- 20 MW of neutral beam injection (NBI).
- 6 MW via ion cyclotron resonance heating (ICRH).
- 6 MW of electron cyclotron resonance heating (ECRH).

This heating power plus magnetic coils are fed by three large flywheel generators that can reach 580 MVA as a pulsed power supply.

2 Theoretical Background

One of the main issues that nuclear fusion faces to be an energy source is the confinement of supra-thermal particles, or also called fast ions inside the chamber. These are high energy particles, which escape the magnetic field lines, going towards the reactor wall, causing structural damage by degradation.

Also, these particles are the fuel ignition of the nuclear reaction, considering that they have enough energy to overcome the electrostatic repulsive forces and fuse.

Therefore, the way to increase the confinement of these particles would start by having a complete knowledge of their instabilities during a pulse and distribution in the plasma.

For this full characterization, the Imaging Neutral Particle Analyzer (INPA) [19], [19] combines the concepts of previous diagnostics, as Fast Ions Loss Detector (FILD) [20] and Neutral Particle Analyzer (NPA) [21], to measure the energy and radial position of the fast-ion population in plasma.

This diagnostic will complete the measurement of the fast-ion phase space distribution to understand the transport mechanisms of these particles and provide a better control of them.

2.1 Motion of charged particles in an electromagnetic field

Fusion plasma cannot be described by ordinary fluid equations because of this low density. Hence, single-particle movement and effects created by collective interactions are the main response of the system dynamics. For the scope of this project single motion of a charged particle in an electromagnetic field has been considered appropriate for the description of this diagnostic.

The magnetic confinement approach takes advantage of the electromagnetic properties of the charged particles of the plasma to guide their motion and confine them without any mechanical barrier. This motion is described by Lorentz's force [22], presented in Eq. (2-1)

$$\vec{F} = q\vec{v}x\vec{B} \tag{2–1}$$

where $\vec{F}$ is the force applied on the particles, q is the electric charge, $\vec{v}$ is the velocity of the particle and $\vec{B}$ is the magnetic field.

On Figure 6 the schematic interaction between the charged particles q and the magnetic field $\vec{B}$ can be seen. The particles travel around them in a helicoidal trajectory, axially through the magnetic field lines.

Velocity $\vec{v} = \overrightarrow{v_{\parallel}} + \overrightarrow{v_{\perp}}$, is the sum of the parallel $\overrightarrow{v_{\parallel}}$ and perpendicular $\overrightarrow{v_{\perp}}$ components to the magnetic field.

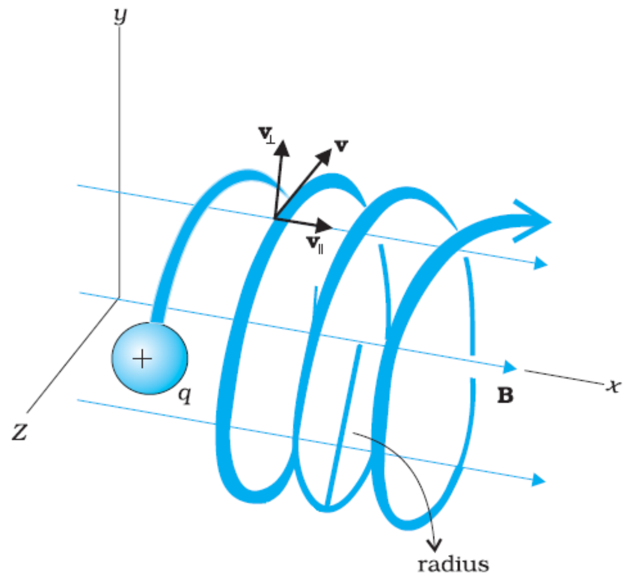

Figure 6 Particle motion in the presence of a magnetic field. Reprinted from [23].

If we consider magnetic fields static and homogeneous the radius of the trajectory, Lamour radius (r_L), and the frequency, Lamour frequency (ω_c), are:

$$r_L = \frac{m \cdot v_\perp}{|q| \cdot B} \tag{2–2}$$

$$\omega_L = \frac{|q| \cdot B}{m} \tag{2–3}$$

where m is the particle mass and $|q|$ is the modulus of the particle charge.

Pitch angle is considered by the relation between the parallel ($v_\parallel$) and the total velocity of the particle (v), defined by:

$$p \equiv -\frac{v_\parallel}{v} \tag{2–4}$$

Finally, to define the particle phase space four parameters are required:

- Major radius (R): Distance from the particle to the torus axis of the tokamak.
- Height (z) located in the midplane of the vessel.
- Velocity (v), presented in Figure 6.
- Pitch angle (p), presented in Figure 6.

2.2 Charge-exchange reaction

The D-D charge-exchange (CX) reaction is the physical mechanism used to obtain information to the confined plasma ions in several diagnostics. One of them, the INPA, the diagnostic presented on this project.

This reaction provides information about the confined fast-ions population, supra-thermal particles, demanded to be measured by the INPA diagnostic. These high energy particles are essential for the ignition. And the CX reaction the perfect way to extract information about them without affecting the plasma.

In Figure 7 the interactions between an ion and a neutral particle that take part in this process are presented, where an electron from the neutral is transferred to the ion, and no momentum or energy is transferred.

$$D + D^{+} \rightarrow D^{+} + D^{*} \tag{2–5}$$

asterisk denotes exited state. Similar to billiard balls, the new neutral (the old ion that get neutralized with the electron during the interaction) escapes to the magnetic field confinement, with its previous trajectory, carrying on all the physical information about the old ion and the neutral losses its excited state by emitting a photon. This new neutral is the Fast neutral marked in blue in Figure 7, being captured by the INPA diagnostic.

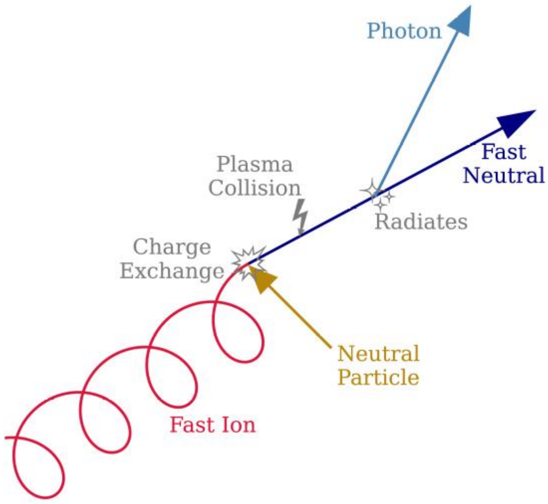

Figure 7 Illustration that represents the charge exchange reaction. Reprinted from [24].

2.3 External heating sources to create fast ions

As previously described, AUG disposes of different systems to generate external heating sources, two of them create fast ions:

- Neutral beam injector (NBI): Small accelerators that provide torus neutral particles of high energy to the torus. In AUG, H^{+} or D^{+} are accelerated, depending on the experiment.

  When the NBI starts its operation, neutral particles in high energy get injected into the plasma, suffering a CX reaction. During this process, these particles get ionized, becoming new fast ions with the same velocity, kinetic energy, produced by the NBI, producing the heating of the plasma.

  In Figure 8, it is presented where INPA is located to study the CX produced by the **NBI#3** with an energy range from 20 to 60 keV.

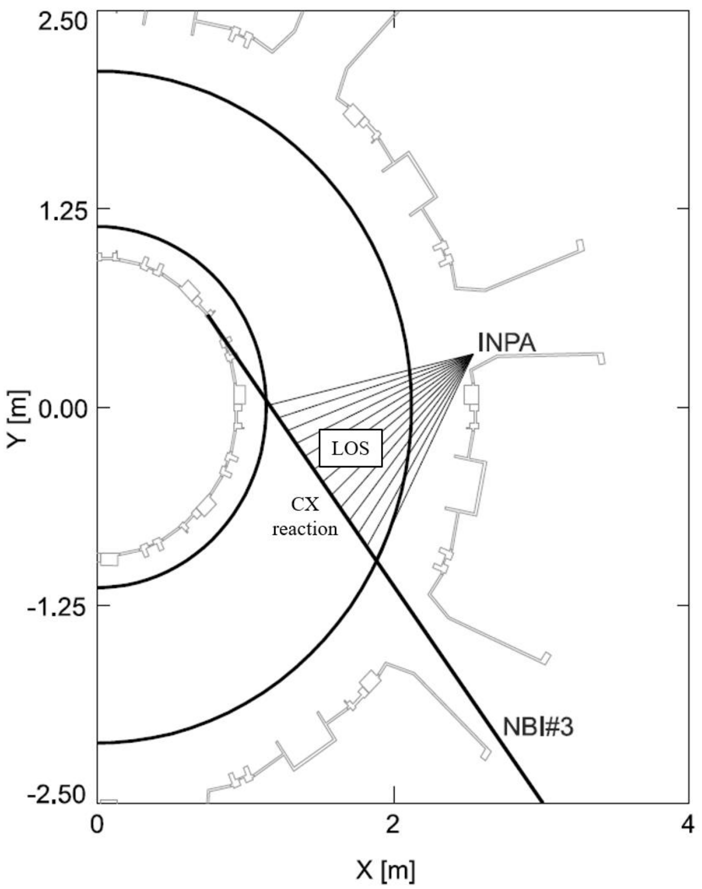

Figure 8 Line Of Sight (LOS) explored by the INPA in its simulated detector position. Top view from ASDEX Upgrade. Reprinted from [25].

- Cyclotron resonance heating (ICRH): No particles are injected. Electromagnetic waves are used to energize particles. This heating is out of the scope of this project.

3 DESIGN DESCRIPTION OF THE INPA DIAGNOSTIC

The INPA diagnostic studies the energy and pitch of the neutral flux, image (c) in Figure 9, that escape from the magnetic field created in the CX process. These neutrals have the energy of the old ions that took part in the CX reactions. Radial position is resolved by the interaction between pitch angle and the several areas of the plasma in the CX reaction that are visible from the INPA. These are the LOS (lines of sights).

The theoretical principle of this diagnostic starts with an aperture (pinhole) in the system that allows the entrance of the neutral particles produced during the CX process, Figure 9.

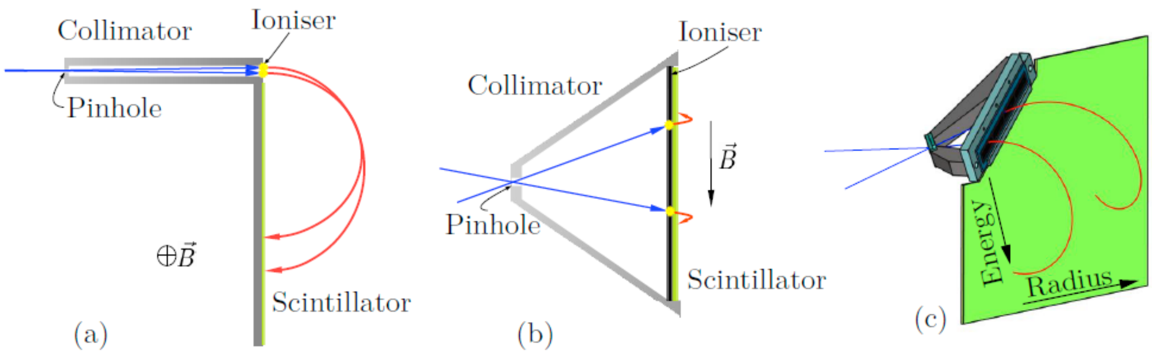

Figure 9 Scheme of the INPA working principle. In blue is the trajectory of the neutral particle, while in red is the trajectory of the ion. (a) and (b) show the side and top views, respectively, while (c) shows a 3D sketch. Reprinted from [26].

Opening the AUG machine, the INPA diagnostic was installed in the ASDEX Upgrade tokamak. Installed in the upper horizontal port, its position is strategically located to a localized sight of the NBI3 beam, as shown in Figure 10, where an overall INPA design description is presented.

The commissioning and first operation have been successfully performed in the AUG experimental campaign 2022, and new publications are expected after the experimental data is analyzed [27].

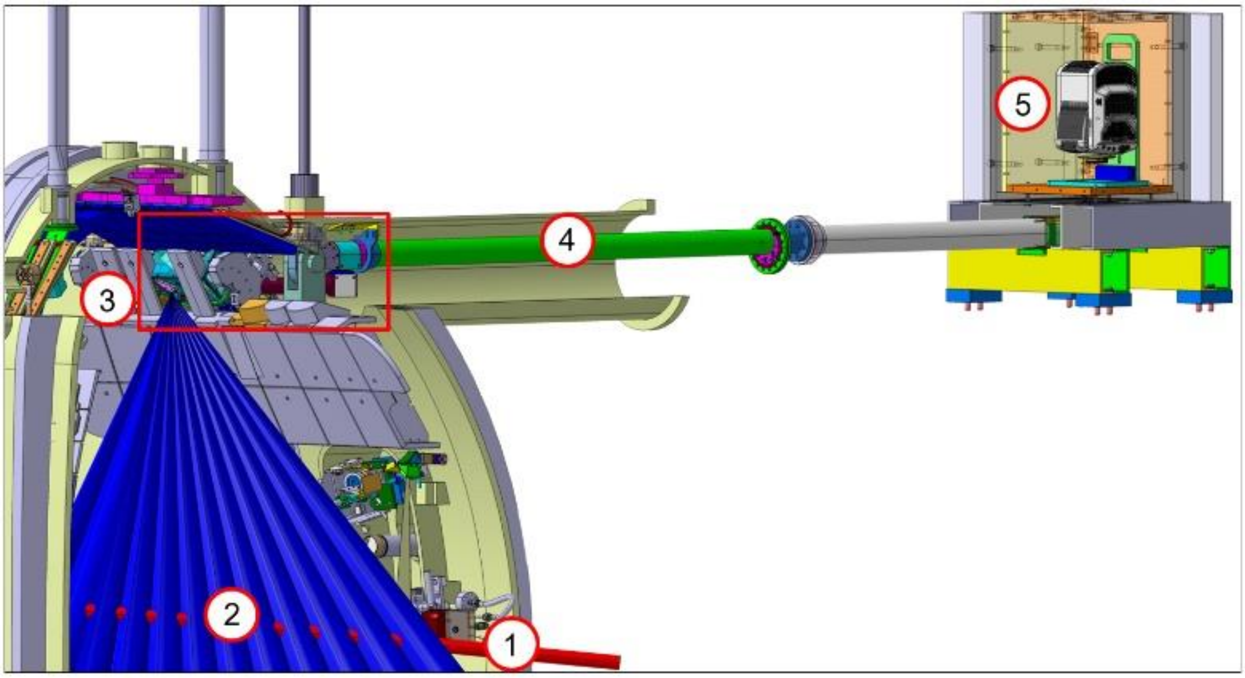

Figure 10 Overall INPA design description: (1) NBI beam, (2) intersection between lines of sight and NBI beam, (3) INPA head, see detailed view in Figure 11, (4) tube with the optical system inside, (5) fast camera. Reprinted from [28].

The operation of the INPA diagnostic is undertaken during the CX process among the neutral particles injected by the NBI and the ions of the plasma. The CX neutral flux aligned with the INPA will be captured by a collimator ubicated in the head (detailed in Figure 11), where they get collimated, ionized by an ultra-thin carbon foil of 20 nm thickness and 56 mm length (see Figure 12).

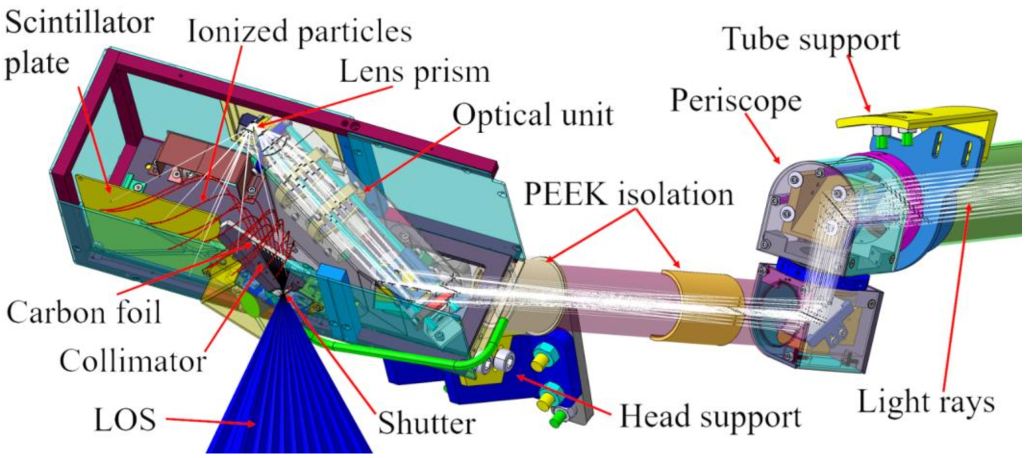

Figure 11 Detailed section view of number 3 in Figure 10, INPA head design according to its performance. Reprinted from [28].

After being ionized and due to the magnetic field, particles change their straight trajectories to helicoidal ones, being dispersed in different areas of a scintillator plate, depending on their radial profile and energy [18]. The size of the scintillator plate covers the maximum area allowed by the space limitation with the surrounding environment. A bigger spectrum of radial profiles and energies are directly proportional to the size of the scintillator plate and, therefore, to the signal quality.

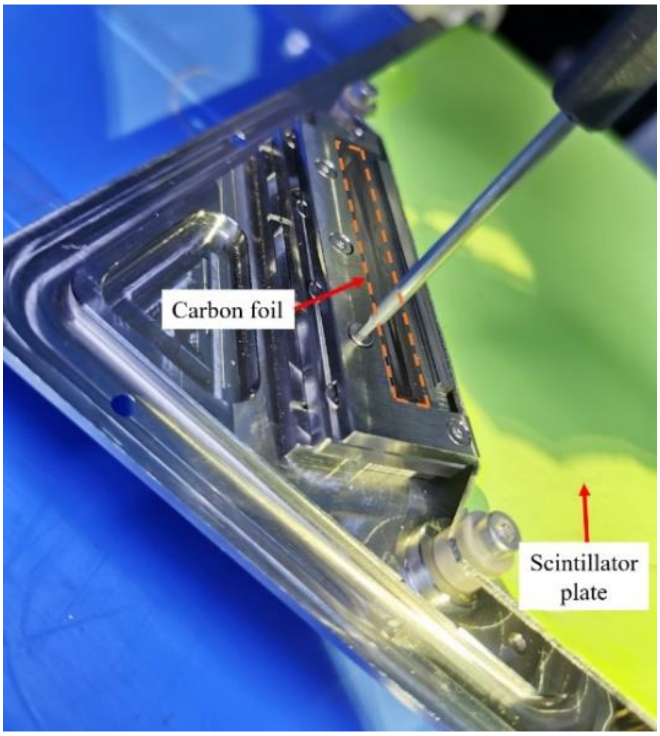

Figure 12 Ultra-thin carbon foil, (20 nm x 56 mm x 6 mm) and scintillator plate (yellow surface, TG-Green). Reprinted from [28].

These particles radiate light (550nm [29]) during the collision with a scintillator material, TG-Green [29], and this signal is guided by an optical path, Figure 10, point (4), made of a set of mirrors and lenses that carries the light emitted up to two acquisition systems located out-vessel, (photomultipliers (PMT), and a fast camera model Phantom V2512).

With the camera, the scintillator can be measured in the kHz range, with a spatial resolution below 1mm in the area around to the optical axis (with a plasma core around 75 keV) and 3 mm in the field of view (FOV) bounds. We obtain a phase space resolution of 12 keV and 7 cm [18], in the optical axis.

Every PMT is an array of 16 channels, each of them covering a surface of 2 cm^2. This area, combined with the high yield of TG-Green and the high gain of the PMT grants a resolution of MHz.

As it can be seen in Figure 13 the fast camera is installed inside of a shielding box designed to minimize several effects that can damage the camera:

- The effects of neutrons: Using layers of PE (polyethylene) with boron, neutrons slow down their energy [30].
- The effects of magnetic field: The box is made of mild steel to absorb magnetic field lines and do not let penetrate inside shielding, leaving the sensors and the power supply in a safe place [31].

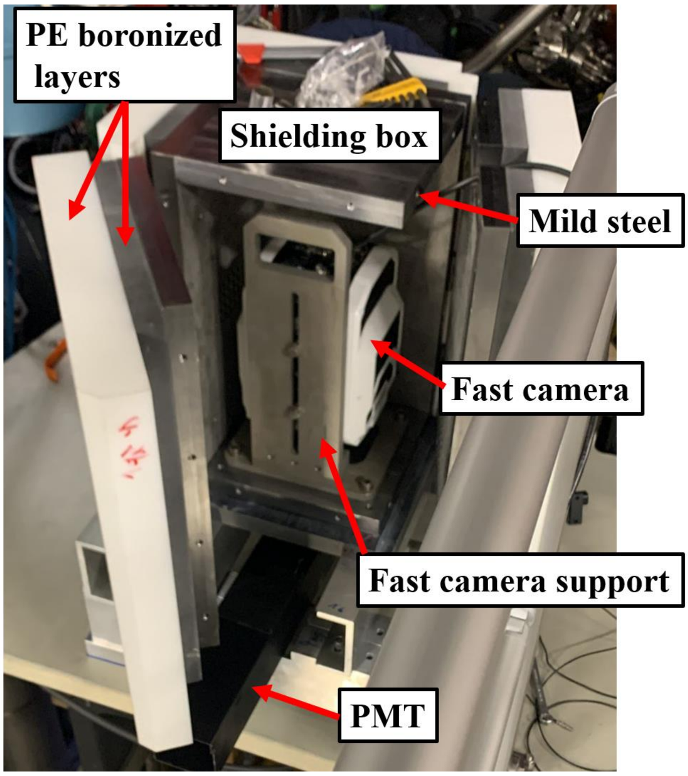

Figure 13 Fast camera being installed inside the shielding box.

4 MECHANICAL ASSEMBLY & INSTALLATION

This chapter presents the influence of several aspects in the design of this diagnostic for a good compatibility during the assembly process, such as difference between CAD and reality, spatial restrictions, electric arcs and high precision for the optical and mechanical alignment. To solve this a series of degrees of freedom have been created to overcome possible uncertainties.

The restrictive volumetric space to install the diagnostic and the demand to not to surpass a system of boundaries based in a color scale, Figure 14, (different limited areas to avoid electric arcs and possible uncertainties between CAD and reality) requires this diagnostic to be designed from the beginning optimizing the space and giving a bigger importance to the assembly. From that point it was decided to build the diagnostic as a modular system to be assembled, following the restrictive route created by the volumetric boundaries in-vessel. The procedure starts inserting from the ex-vessel side, the upper part of the periscope with the long green tube, point 4 in Figure 10. Inside the vessel was installed the lower part of the periscope connected with the red tube to the head, presented in Figure 11.

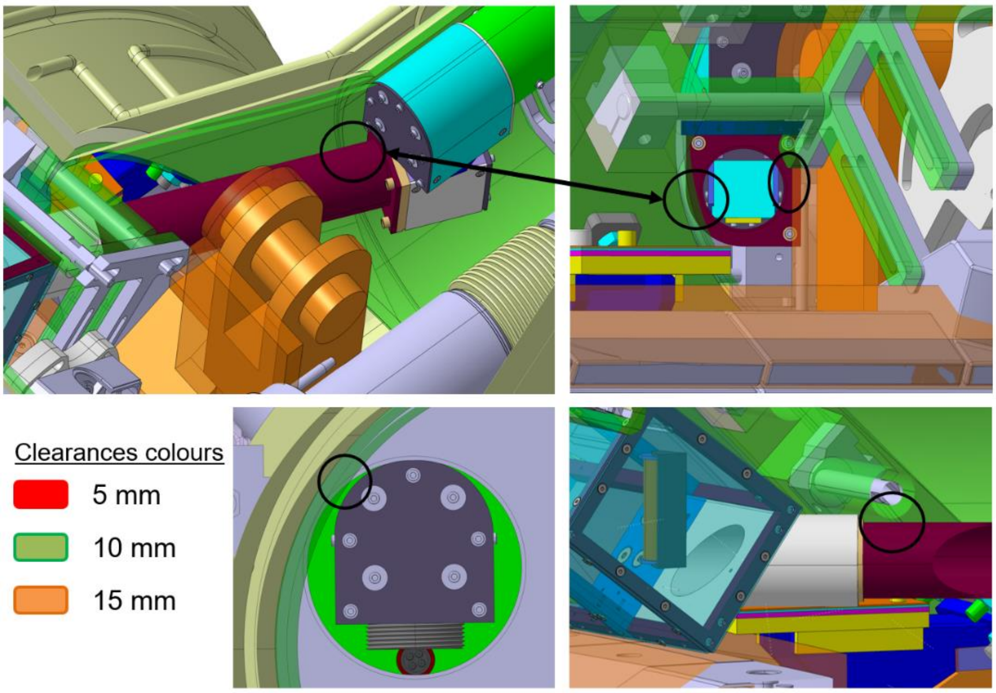

Figure 14 Collage of different views of the INPA head and periscope, exposing with black circles the spatial restriction using a clearance color system.

The complexity of developing this diagnostic, from the mechanical point of view, lies in the interrelation between various aspects, which when one changes influences the rest. These are:

- Differences between CAD and reality: AUG engineers guarantee a precision of 1 cm as the maximum deviation between the CAD environment and reality of any component of the reactor. INPA head is pretended to maximize the volume, as it is directly related to the quantity and quality of the received signal.
- High spatial restriction: Figure 15 illustrates how the INPA head is positioned between two diagnostics on its sides, coils in the lower parts, the wall of the chamber in the rear part and the front part rubbing against graphite protections (pink plates) that protect it from plasma exposure. The size of the head is very limited.

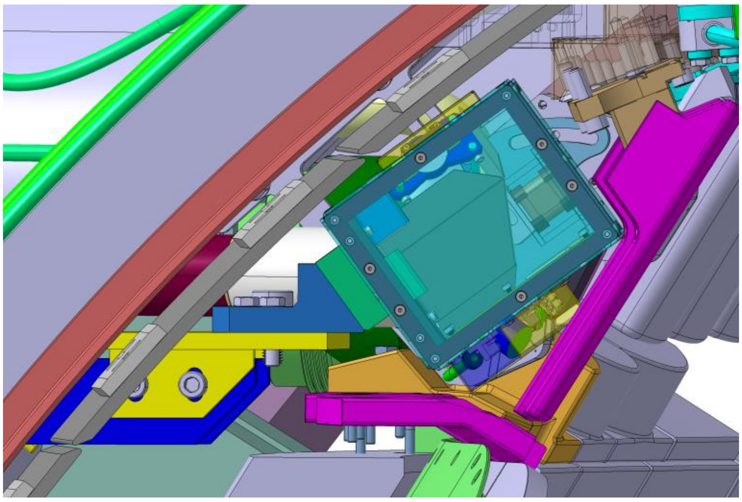

Figure 15 Lateral side of the INPA head showing the environment that delimitates the head size.

- Assembly process: The assembly process is key in the design as it is affected by the spatial restrictions that do not allow the entire system to be installed from outside the chamber, through the port. It is also necessary to note that there are two in-vessel supports that transmit the weight load to the reactor structure and the forces induced by electromagnetic events, so it is necessary to work from inside the reactor.
- High precision in optical alignment: The optical system was designed from lenses and mirrors for a higher spatial resolution of the signal if we compare it with a fiber optic bundle. This approach has the disadvantage that, being a system influenced by the position of each of the frames of the elements that make it up, the sensitivity of losing one of the 6 optical axes that make it, due to an imprecision failure in the mechanical design. is very high and loses much of the transmitted signal. It is also necessary to highlight the points described above, where we see that the assembly is modular and must be assembled inside a reactor with difficulty of work and position uncertainties of all the components that surround it.
- High precision in mechanical alignment: As can be seen in Figure 10, the head of the INPA, point 3, has to be aligned with the NBI3 beam in order to obtain the LOS of the CX reaction. To do this, the collimator is in the same plane as the NBI3 beam, the pinhole and the carbon foil must be in the same plane, so any modification of the ideal position must be oriented to the NBI3 beam.
- Electric arcs: The diagnostic is required to avoid electric arcs of different distances depending on the component that is exposed, based on the color scale presented previously in Figure 14. In areas where these distances could not be met, it was decided to use PEEK insulating material to avoid the arcs [32].

The solution treated was the use of a set of degrees of freedom (DOFs) to absorb possible mitigations and for not let then impact on the rest of the properties.

The periscope is shown in Figure 16, where it is in charge of giving these two DOFs to the system. It is prepared to manually modulate its height by 1cm, without affecting on the optical signal, and a rotation of the axis in the lower part of the periscope in the toroidal plane, causing the rotation of the optical image with no effect in misalignments or optical distortion. To do this, the head support provides the same DOFs so that the position of the head, which is connected to the periscope, can be adapted to any configuration adopted as the position between the INPA head and its support is not determined until the calibrations.

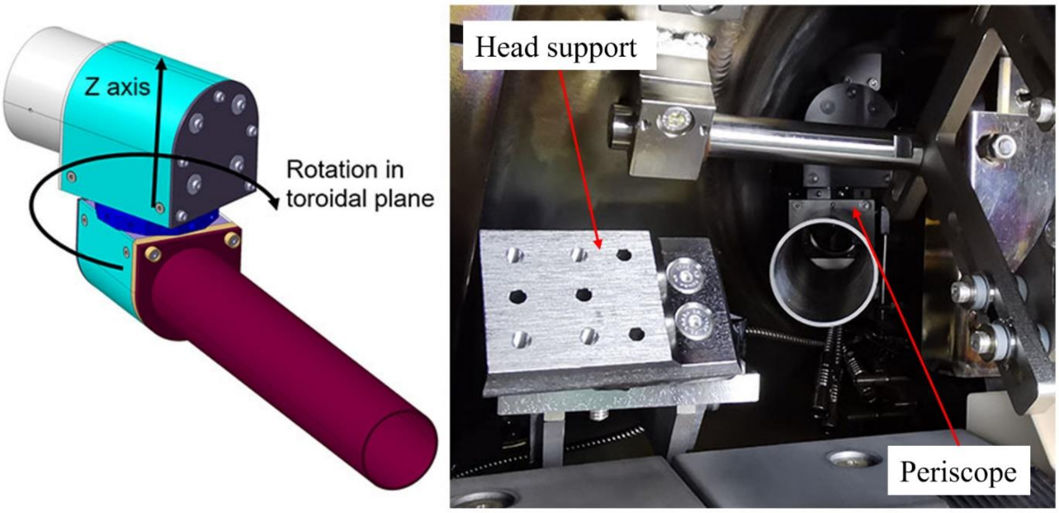

Figure 16 Left image, CAD of the periscope with its degree of freedom. Right image, real image of the head support and periscope position.

A 3D printed system with 3 laser pointers was allocated inside the INPA head, in the ultra-thin carbon foil position, oriented by the straight path of the CX neutral flux coming towards the collimator. With these pointers and the help of the DOFs (periscope movements) the head was adjusted to align the plane formed with the collimator and the line of the NBI3 beam, including the pinhole with the collision of the NBI3 beam and the plasma center.

When the diagnostic is assembled, the optical system is checked to see if the results are the same as in the calibration lab. Then, the diagnostic is prepared for the mechanical calibration. Note that with the DOFs of the periscope there is no modification of the optical system when the mechanical calibration is being made. The periscope absorbs movement turning the signal, something that does not affect the results. The INPA head is mechanically aligned when a set of lasers, installed in the collimator plane passing through the pinhole, match with the NBI beam (position indicated by a white rope in Figure 17). In this figure, the laser illuminates the rope showing a good agreement in the alignment. Blue cones are the CX neutral flux in CAD figure and red lines determine the diameter of the NBI3 beam, superimposed to the image, for a better comprehension.

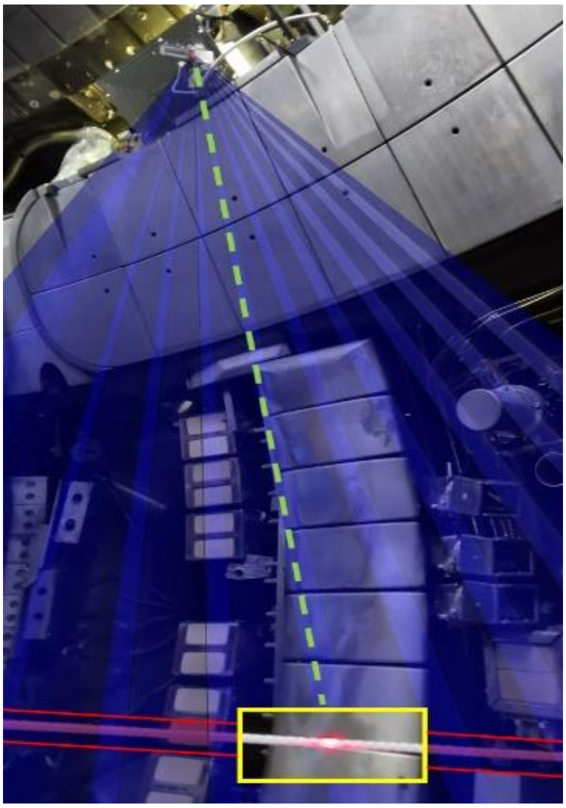

Figure 17 Match between the NBI injection line and the central pointer of the series of lasers positioned inside the INPA head during the installation/alignment process. Reprinted from [28].

5 OPTICAL SYSTEM

5.1 Description

INPA's optical system is characterized by the space limitations and the assembly process described in the previous section. To settle this question, the use of a fiber optic bundle that could conform the three-dimensional constraints, leaving the mechanical calibration independent of the optics, was proposed from the beginning.

By virtue of the degradation of the optical fiber produced by neutrons, which are produced in the fusion reactions, the low spatial resolution collected when producing the image and the difficult access for a possible replacement, this possibility was excluded. As a solution, a system composed of a custom prism, 3 mirrors, 6 lenses, a beam splitter, and 2 sensors acting as the objects, represented the overall INPA optical ray tracing simulation in Figure 18.

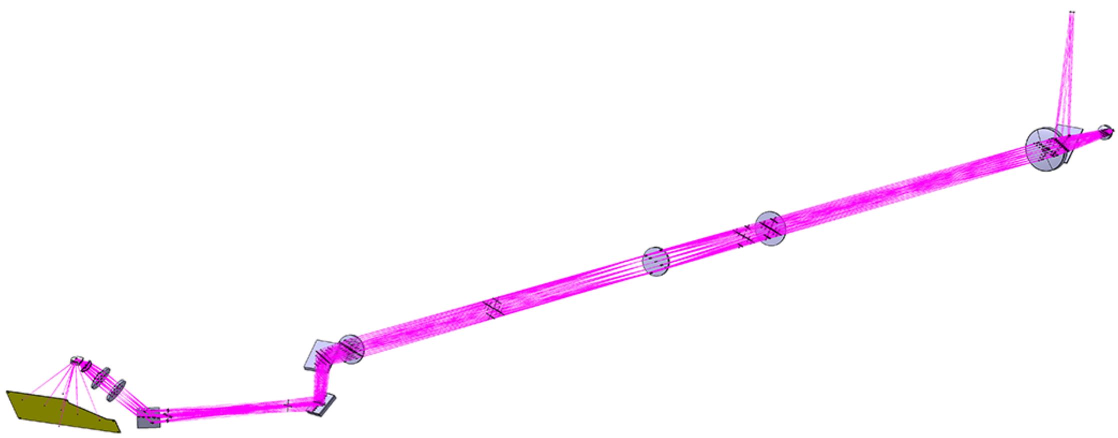

Figure 18 Overall INPA optical ray tracing simulation modeled by Zemax [33].

For the transmission of the light from the image (in-vessel) to the objects (out-vessel), 6 optical segments that are connected in a three-dimensional sequence are required in a modular system compatible with the assembly process.

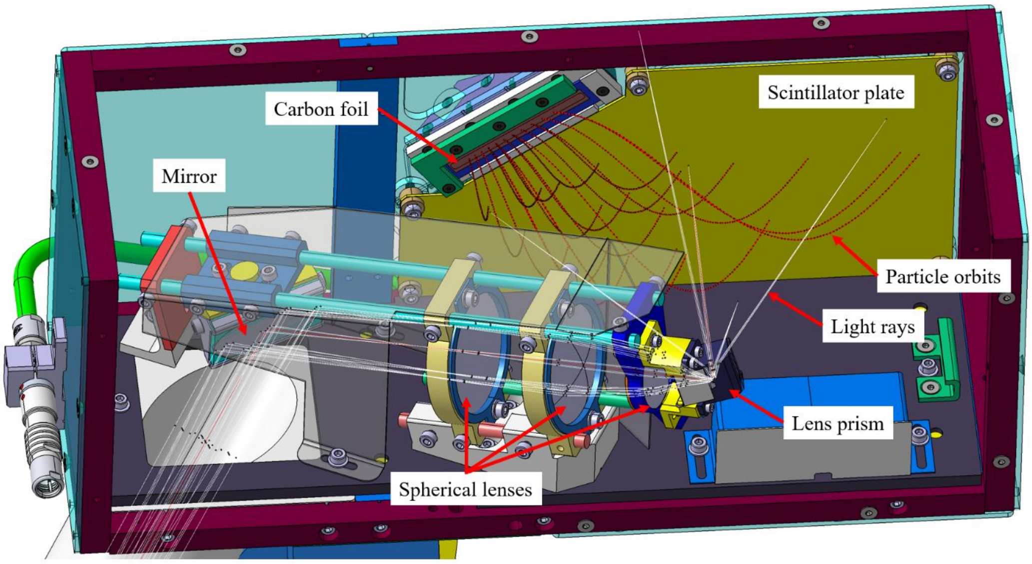

Figure 19 Rear side of INPA head shows the limiting space between first lens and scintillator image.

The image transmitted (scintillator plate) is produced inside the head, where particles collide with the scintillating material. This plate is positioned by the NBI 3 beam and oriented with the magnetic field lines.

Considering INPA head dimension is limited, as can be seen in Figure 15, by the minimal distance allowed to the graphite protection for the chamber wall (grey plates) and the graphite plasma limiters (pink plates), it causes a limited distance between the scintillator plate and the first lens, less than 9 cm, Figure 19.

This distance determines the image area that the optical system can transmit, named as the Field of View (FOV), characterizing the signal quality. A customized prism as the first lens, shown in Figure 20 was designed, and manufactured, allowing a field of view (FOV) that covers the main area of the scintillator plate. Barrel distortion has been promoted creating a panoramic view of the image for increasing the FOV diameter to 140 mm.

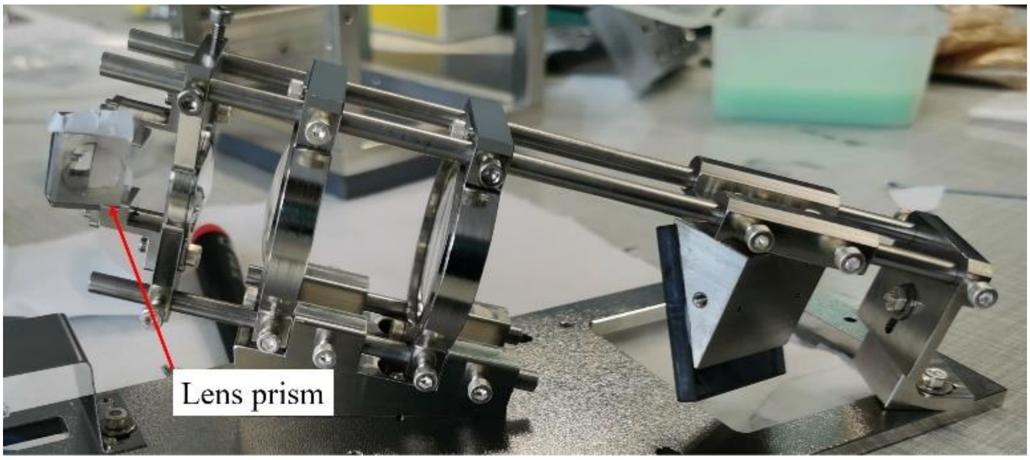

Figure 20 Lens system module in the INPA head. Lens prism is shown as the first lens of the optical system. Reprinted from [28].

The lens prism is the first element of the optical path. Its first surface is a spherical one which collides with rays from the scintillator image and transmits to the second surface, that reflects in 90 degrees as a mirror. This allows to drive the optical path respecting the head mechanical boundaries.

After the lens prism a set of three lenses rearrange the diameter of the image, shown in the ray tracing below, and transmit the image that is reflected to a mirror who changes the optical path direction to enter in the periscope.

The periscope is a set of two mirrors tilted 45 degrees to the optical paths and parallel between them to transmit the light increasing the height of the image position. Then, a tube of 1,6 m length, with two lenses inside, connects the periscope to the vacuum window transferring to the out-vessel side, where the image is split and readapted with lenses for two different acquisition systems, a fast camera, and a set of PMT (objects). Optical elements are described in Table 1.

Table 1 Optical elements

Item	Radius (mm)/ Dimensions (mm)	Focal distance (mm)	Coating
Prism	6	-	MgF2 & *Enhanced Aluminum*
Lens0	25	35	YAG-BBAR
Lens1	46	400	MgF2
Lens2	46	400	MgF2
Lens3	50.8	400	MgF2
Lens4	50.8	400	MgF2
Lens5	50.8	800	MgF2
Lens6	76.2	250	MgF2
Mirror 0	40x40x8		*Enhanced Aluminum*
Mirror 1	60x45x8		*Enhanced Aluminum*
Mirror 2	60x45x5		*Enhanced Aluminum*
Beam Splitter	50x7x3	50% reflection/50% refraction	

5.2 Optical alignment

Thanks to the free movements in lenses and mirrors, in a three-dimensional optical system, during optical alignment, the modularity of the system has been an advantage to calibrate each set separately and later the whole set. Taking 3d printed targets, Figure 21, with a hole and pointer lasers, has been performed the calibration emulating the optical axis for each module.

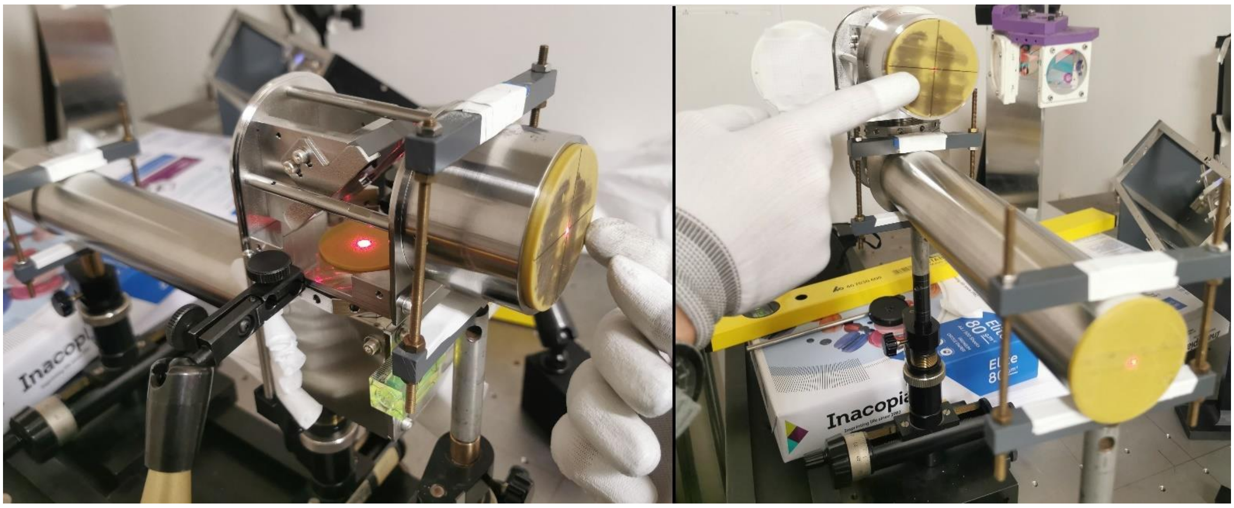

Figure 21 Optical alignment: to the top periscope part in left image, to the complete periscope (top and down modules) in right image.

In the periscope, the upper mirror was positioned and oriented using an adjustable support transmitting the optical axis over the center of the 3d printed target as shown in the image on the left. In the image on the right, it is shown how the laser enters in the upper part of the periscope and exits through the hole in the target at the bottom of the periscope, signal that means the two mirrors are calibrated.

To align the head optical component a system with guide bars holds the lenses and mirror to freely adjust the system and maintain the components in the same optical axis. The mirror can also turn perpendicular to the optical axis to match the angle with the optical axis of the periscope.

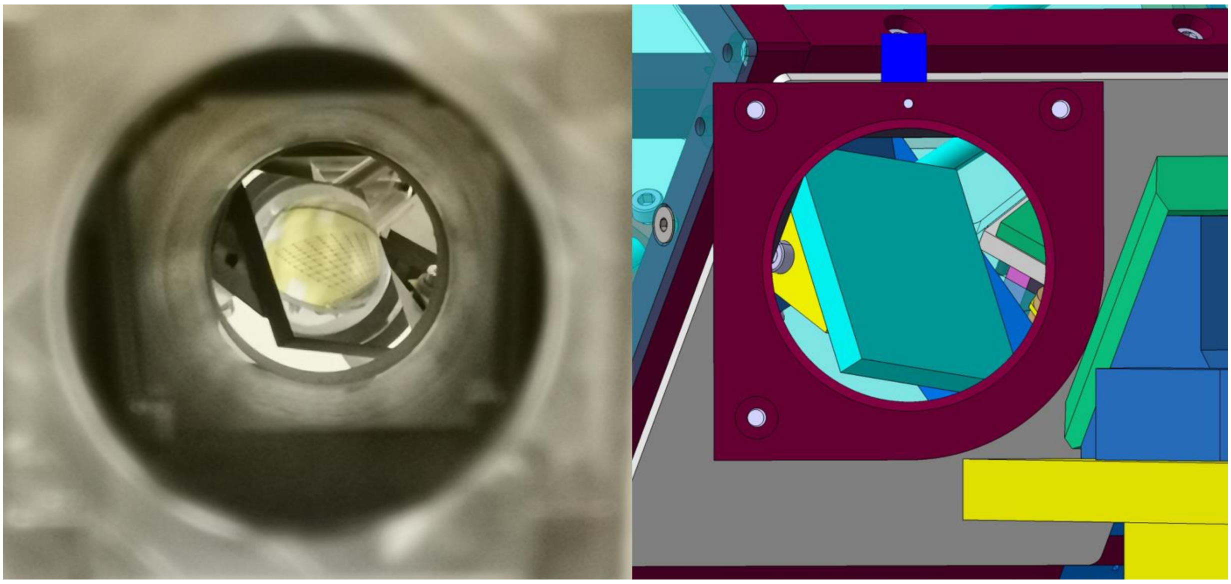

Figure 22 Left image, a photo taken after optical alignment of the head and periscope, with conical perspective. Right image, a CAD image of the INPA head in parallel perspective.

Once the periscope is aligned the head needs to be connected to the periscope to use the same path and the laser on the optical axis. As a result, Figure 22 shown differences between reality in left image, photo taken after periscope, in conical perspective, of the camera, and CAD design in right image in parallel perspective. In the real image appears the mount of the mirrors and lenses and the strike-map of the scintillator plate transmitted by the optical path, signal that is perfectly aligned.

Considering the access restrictions to the long tube connected to the port, the 2 lenses inside are fixed between internal tubes, Figure 23. Axially cut with an accurate tolerance to avoid movements.

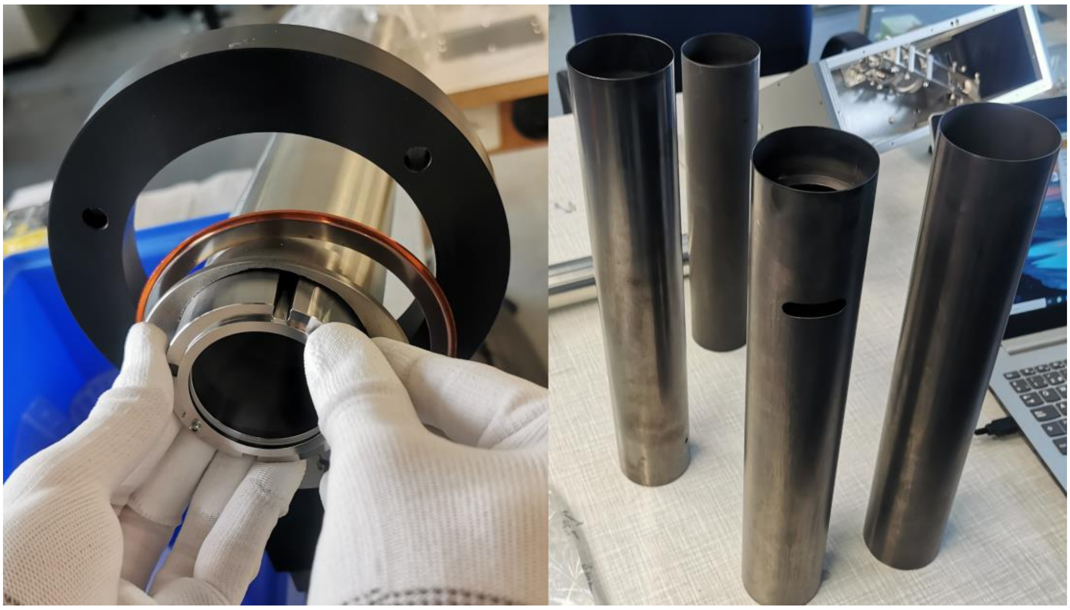

Figure 23 Left image, introducing the lenses with their mounts. Right image, tubes accurate in height to maintain and fix the distance of the lenses.

For the total alignment, a laser has been positioned in the out-vessel side, at the camera sensor location, in the optical axis, pursuing the reverse optical path of the signal.

The theoretical position of the optical axis is painted as a reference with a red dot over a strike-map sheet added to the scintillator plate, (red dot at Figure 24 left). The laser reaches exactly at the red dot named before (red light at Figure 24 right) solving the system with a perfect alignment that matches with the theoretical one.

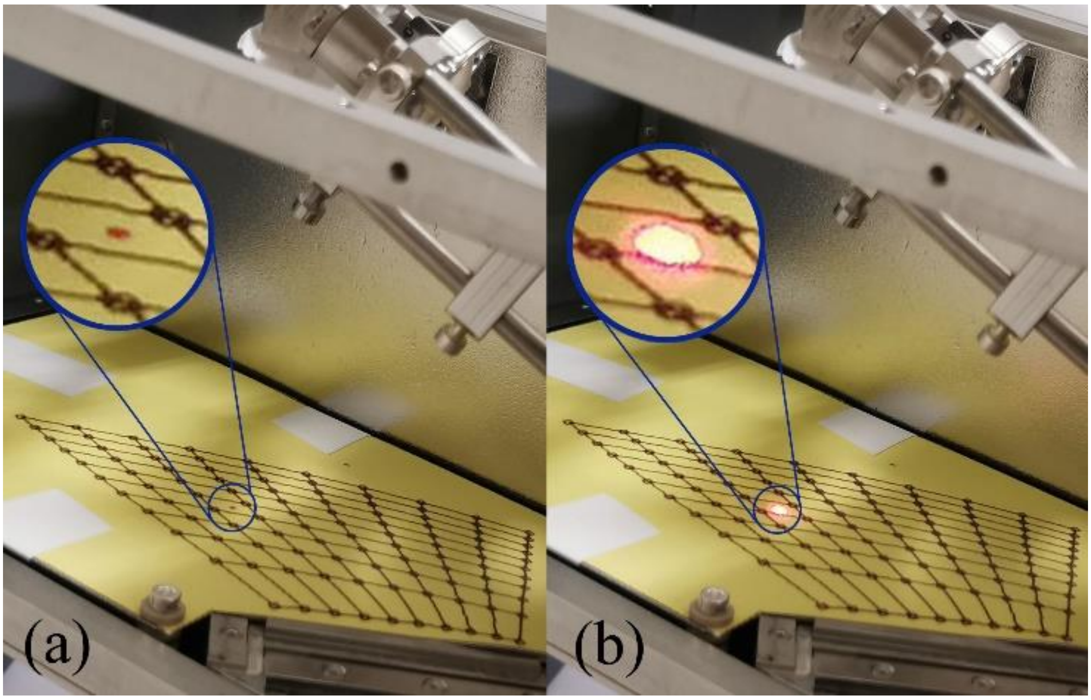

Figure 24 General optical alignment using axis position in scintillator plate: (a) theoretical with marker red dot (b) experimental laser red light. Reprinted from [28].

5.3 Optical simulations

The barrel distortion, Figure 25, applied on the curvature of the first prism surface was encouraged in the design to increase the Field of View (FOV) of the transmitted signal in the optical design. This distortion must be eliminated in the data post-processing so that the processed data is in optimal condition.

For this reconversion of the image, the theoretical values obtained with the Zemax software [34] and the real values measured with the fast camera should be compared to the position of a sheet of paper with a 1cm spaced grid placed on top of the scintillator plate.

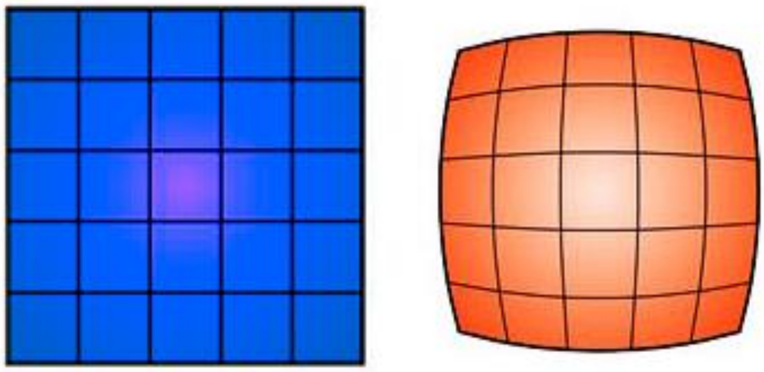

Figure 25 Left image, grid with no distortion. Right image, grid with barrel distortion.

Figure 26 in the lower left corner the grid is shown on the scintillator plate taken from the camera. The barrel distortion can be seen from the view of the scintillator shape. The red dot marks the optical axis and has been made to coincide with one of the corners of the grid. All the blue points highlight the corners of the grid, to measure and represent on the graph, decrease in distance when moving away from the optical axis, produced by an increase in distortion, as predicted by Zemax.

The distortion values were obtained using the equation $Dist = (d - dr)/(dr)$, where d is the real distance between two points and dr is the distance measured in the image taken by the camera, (distorted distance).

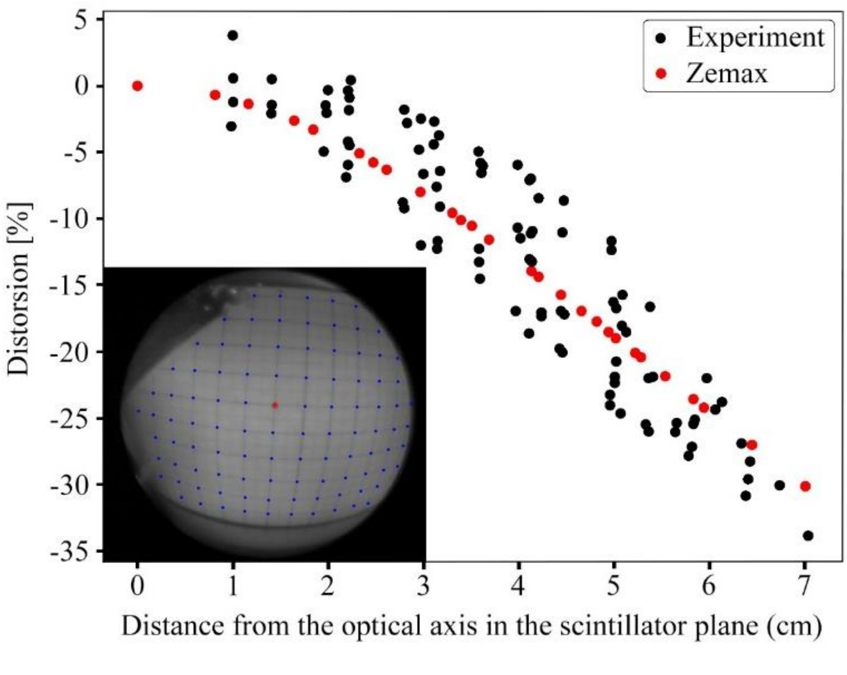

Figure 26 Correlation between the simulated and experimental barrel distortion, increasing with the distance to the optical axis (FOV center, red dot). Reprinted from [28].

Figure 26 shows the results obtained where we can recognize the correlation between the experimental and theoretical values.

Therefore, we conclude the theoretically obtained curvature lines with the Zemax software can be used to flatten the image and obtain a distortionless image during the post-processing data analysis.

5.4 Optical transmission

The transmission factor (the proportion of light that actually arrives to the sensor) depends on the solid angle that the system can cover from the image, and also, on the number of lenses, the glass materials and the coating used. These characteristics are evaluated as a reduction of the transmission due to the surface reflections.

5.4.1 Solid angle:

Solid angle (Ω) is a 3D angular volume. The angle at the center of a sphere intersects by a part of the surface equal in area to the square of the radius, Figure 27.

A steradian (sr) is the unit of the solid angular measure. Defined as conical in shape.

$$\Omega = \frac{A}{r^2} \tag{5–1}$$

In our system, solid angle is the amount of the field of view, in a particular point of the scintillator plate that the prism covers.

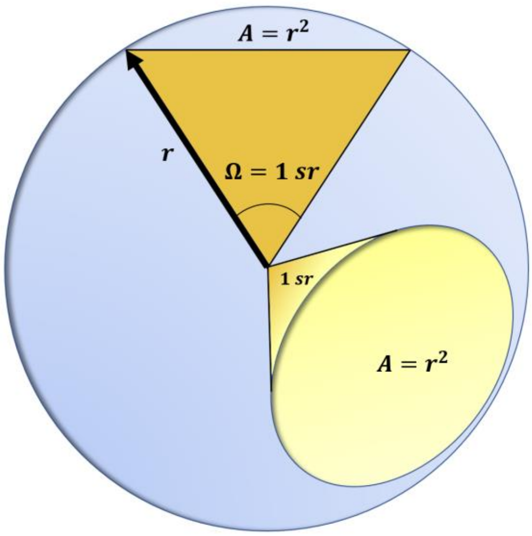

Figure 27 3D representation of solid angle in a sphere (blue circle).

5.4.2 F-number

F-number is an adimensional number defined, as the ratio between the focal length of the system and the diameter of the clear aperture. It represents the reduction of the amount of light entering in the first lens of the system.

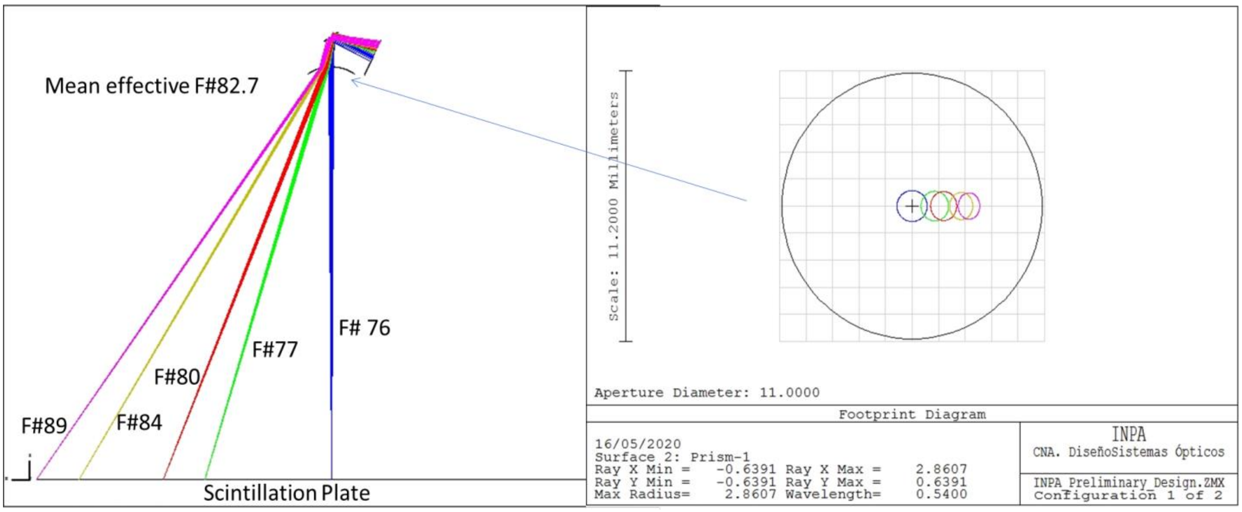

Figure 28 In the left image, F-number in separate points of the scintillator plate. In the right image, representation in the first lens the different surfaces of every solid angle [33].

An average F-number of **82.7** is taken as the representative value for the equations, Figure 28,

$$\Omega = \frac{\pi}{(2F)^2} = 1{,}15 \cdot 10^{-4}\ sr; \tag{5–2}$$

considering R, as the reduction of light by reflections in all lenses and mirror surfaces (80%), the F number translates into a transmission.

$$\mathrm{T} = \frac{\Omega}{2\pi} \cdot R = \mathbf{1{,}4 \cdot 10^{-5}} \tag{5–3}$$

Close to the optical axis, the resolution is 1mm. The system is designed where the maximum signal is expected to obtain a maximum resolution, being that position the FOV center. At the edges, the resolution decreases to 3mm.

5.5 Optical signal result

In conclusion, a comparison between the expected synthetic signal, left, (simulated INPA signal and strike map) and the optical real, right, is presented in Figure 29.

The right image is a view of the scintillator plate from the camera with a sheet of paper of the strike map fixed over the scintillator plate, to see the correlation obtained. It is expected to reach signals similar to the theoretical one to a high performance of this diagnostic.

In Figure 29, we can visually verify that the calculations of the previous sections demonstrate that the quality of the signal is quite high despite the intricate design. It can also be noticed that the optical signal has a certain roundness, as if it were bulged. This has been explained in section 5.3 where we promote barrel distortion and increase the FOV. Later, during the post-processing of the received signal, with the results of Figure 26, said distortion is eliminated to have an image very similar to the synthetic one.

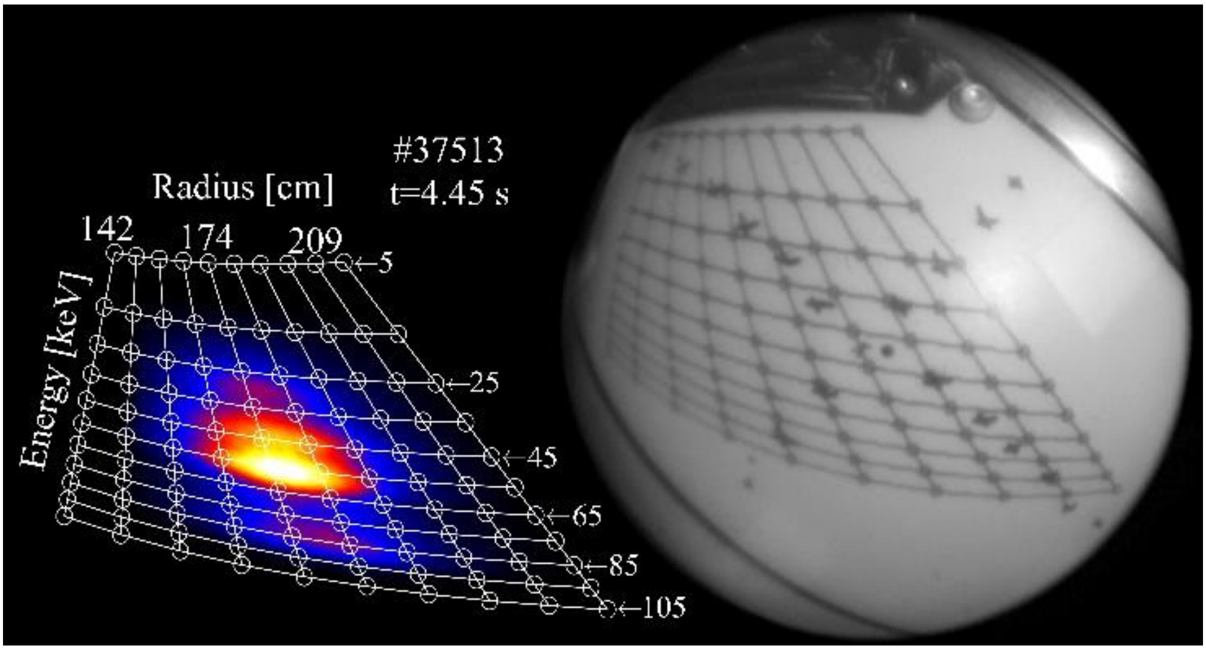

Figure 29 Analogy between the synthetic signal used as the input model (left strike map) and the real image captured in the final optical alignment and assembly done, with a strike map sheet paper on the scintillator plate as the object (right). Reprinted from [28].

6 STRUCTURAL INTEGRITY

This chapter will be a comprehensive explanation of the main analysis carried out to validate the integrity of the design. Therefore, a set of finite elements analysis has been done to simulate the different interactions that the system manifests with the environment. First, an electro-mechanical (EM) analysis of different phenomena that happen in a tokamak, together with the required theory for its understanding. Afterwards, a thermal analysis to check if the interactions between particles and the INPA head exposed to thermal heating, exceed the temperatures allowed by the materials used.

6.1 Finite Elements Analysis input

The INPA structural integrity system has been determined applying Finite Element Analysis (FEA) to provide a safe operation system over the worst-case scenarios. Joints between parts in ANSYS Mechanical have been modelled similar to reality. The head support is connected to the vessel, the contact areas are considered fixed supports and also the support of the tube with its C shape.

The majority of the INPA components are made of stainless steel AISI 316 [35]. Material properties used in FEA analysis are presented in Table 2 below.

Table 2 Material properties Sainless Steel 316

Density	7850 kg/m^3
Specific heat capacity	404 J/kgK (@100ºC)
Conductivity	14.7 W/Mk (@100ºC)
Thermal expansion	$15 \cdot 10^{-6}$ /K
Yield strength	290 MPa
Melting temperature	1370ºC

6.2 Electro-mechanical (EM) assessment

6.2.1 Theoretical background

6.2.1.1 Electromagnetic loads:

In tokamaks, the interaction between magnetic fields and electric current creates mechanical forces, giving a strong complexity for the system.

Lorentz's law was previously presented as the equation to determine the motion of changed particle section. For electromagnetic loads, they are no longer appropriate to define the macroscopic interaction of currents flowing through the mechanical components of the system and the magnetic field. For this reason, this equation has been modified taking the electric current $\vec{I}$ as a set of particles in motion.

$$\vec{F} = \vec{I} ds \ x \ \vec{B} \tag{6–1}$$

Where $\vec{F}$ is the force going through the mechanical component and $\vec{B}$ is the magnetic field.

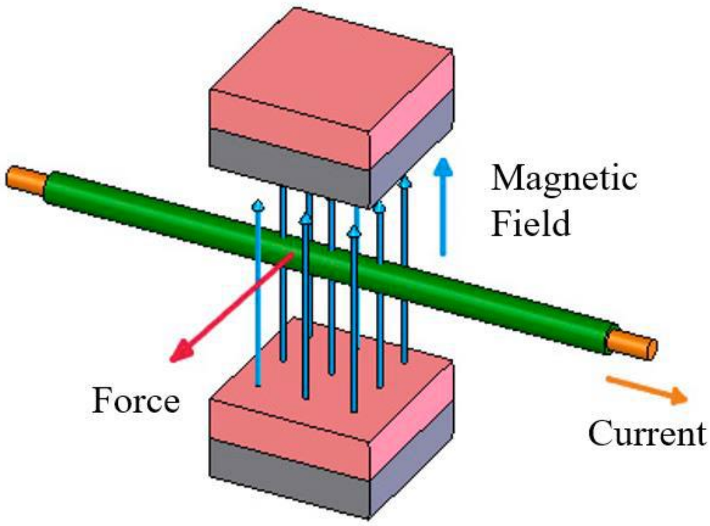

Figure 30 Interaction between magnetic field and an electric current, manifesting a force in the conductor. Reprinted from [35].

Figure 30 presents schematically the induced forces generated from the influence between a current flowing through a wire and a magnetic field. This force acts perpendicularly to the plane defined by the magnetic field and the current [37].

In tokamaks, the components with a major influence of this EM forces are the coils, used to create the magnetic field being fed by an electric current flowing through them, (Biot-Savart's law) [37].

The tokamak components with electrical conductivity suffer EM loads. These are the eddy currents and are solved by Faraday's law [37], which states that the variation of the magnetic field with time ($d\vec{B}/dt$) generates electric current in the surrounding conductive components.

Moreover, these currents are governed by Lenz's law, where the conservation of the magnetic flux in conductive elements originates electric currents, within them, that oppose the change of the magnetic flux. Because these conductive materials also possess some electrical resistivity, energy losses are quickly converted to heat. Therefore, as current flows through the elements, its interaction with the magnetic fields creates forces.

A general overview of this effect is presented in Figure 31:

- (a) shows when the input current is flowing in the coil increasingly, the magnetic flux associated has a positive variation rate. Accordingly, the current induced (eddy current) in those affected by the magnetic flux opposes the input current, and therefore, the variation of the magnetic flux.
- (b) presents the opposite case. When the input current decreases, the induced current (eddy current) opposes the variation of the magnetic flux. This creates a current in the same direction as the input.

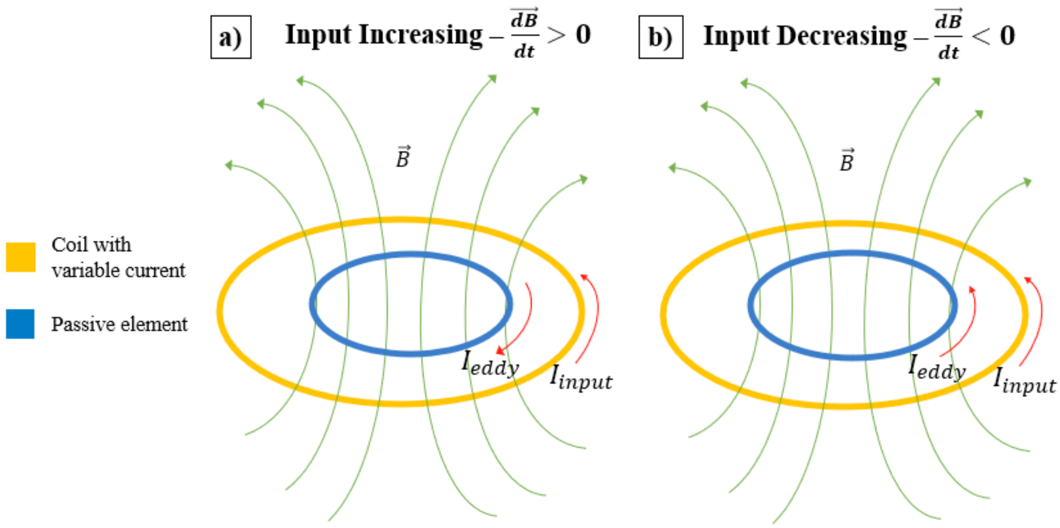

Figure 31 Schemes of the induction of current, yellow ring, in a magnetic flux variation, (a) when is increasing the current, the current induces in the blue ring has an opposite direction to the entrance current, (b) when is decreasing the current the induced current goes to see same direction the entrance current. Reprinted from [38].

The induced current will have a similar direction to the original current that suffers the variation, and its orientation will be given by the sign of the variation of the magnetic flux. This induced current will be proportional to the variation of the magnetic flux. At more aggressive variations higher currents.

In a tokamak, eddy currents are mainly due to variations of the magnetic fields in time, which are associated with electric currents. To a large extent, tokamaks are built with conductive elements that are affected by this variation, inducing in them a current that opposes the variation of the magnetic flux.

Main mechanisms related to the generation of eddy currents in tokamaks are associated with the intrinsic activity of a tokamak and plasma EM events [39]. Several mechanisms are:

- Energization of coils: The variation of the huge currents flowing through the coils from zero to the operational value, generates a magnetic fields variation.
- Plasma breakdown: The most extended mechanism to ionize the particles and create the plasma is varying the magnetic flux of the central solenoid (CS) abruptly.

The other major source of eddy currents is the plasma, whose forces induced on the INPA diagnostic are studied below.

The use of an electromagnetic model has been applied. Feeding all the poloidal and toroidal coils, it has been considered the forces operating on the system by reason of induced currents during the current ramps [40].

6.2.1.2 Disruption event

A large current flow in the plasma to improve its magnetic stability. However, due to fluctuations of the plasma during its operation, it can suffer from extreme EM events that generate a rapid extinction of the plasma current. These events are the Disruptions, and they are the most severe electromagnetic events with respect to the structural integrity of the tokamak [41], so an evaluation of them is required.

The disruption phenomenon is an instability of the plasma, where the particle confinement is destroyed abruptly.

Thermal and magnetic plasma energies are released rapidly. The strength of a disruption is treated by its duration, the shorter, the tougher. In AUG, it is characterized by the quench of the plasma current 760 kA in 5.5 ms [42].

Disruption studies have been accomplished to verify the system structural integrity, because is the critical EM event that can affect the system.

Considering that the magnetic flux does not vary, eddy currents are not induced in INPA. The current during a disruption is assumed to drop linearly, accordingly, the magnetic flux variation keeps constant ($\mathrm{d}\vec{B}/\mathrm{dt} \sim \mathrm{constant}$) along all disruption and the current induced in INPA is maintained equal to that.

6.2.2 Analysis method

Once the different EM events have been described in this section, the method implemented for the resolution of the calculations implicit in the assessment of the EM loads in INPA will be addressed. This study allows the calculation of the induced current due to the variation of the magnetic flux and the associated EM forces. These (volumetric) forces are used to find the stress induced in the detector and thus check the structural integrity.

The EM analyzes developed in this project have been carried out with the ANSYS Maxwell finite element method (FEM) software [43]. It is a software package that, based on the resolution of Maxwell's equations, in a limited region of space, allows the evaluation of electromagnetic problems. The mesh is based on an adaptive meshing process that uses tetrahedral elements composed of 10 nodes. This is allowed to modify its maximum size of the tetrahedrons or the maximum number of geometric elements that compose it. The error limit for these will be 5%.

ANSYS Maxwell is commonly used in the fusion field for the resolution of EM problems, in a similar path to the one presented here. ITER [44], COMPASS-U [45], JT-60SA [46] are tokamaks with a standard use of this software assessment. Hence, it is assumed that the results obtained with this software have been tested enough to rely on it.

Volumetric forces are obtained with this software as the solution for these EM events. To validate the structural integrity of the system another software module is linked to convert the induced forces, applying the geometry and their connections, to the stresses and the strains that the model studied suffers when it is subjected to the induced loads and be compared with the yield strength of the material that are made the diagnostic. This is performed in the FEM software ANSYS Mechanical, which will allow the coupling of both analyses to perform a multiphysics simulation. Moreover, this software has been used to obtain in the thermal assessment the stress and strain produced by the thermal charges in the surfaces most exposed to plasma, obtaining these loads has been described later, in the thermal assessment.

This software has many types of elements, both of first and second order for a diversity of analysis. Users can redefine the mesh in an accurate way, optimizing the computerization time. To check the results, convergence tests will be carried out. The error limit will be the 5%.

6.2.2.1 Eddy currents assessment

For the experimental conditions taken on this assessment, the current ramps that feed all the poloidal, toroidal coils and the solenoid from the discharge #39613, as a representative coil current evolution reference in ASDEX Upgrade. These current ramps feed the coil during a pulse of 7 seconds [42]. Toroidal field coils have the same current and they are constant during the pulse: 1.6 MA. Values are presented in Figure 32. In Figure 33 represent the position of every coil in AUG and the INPA position.

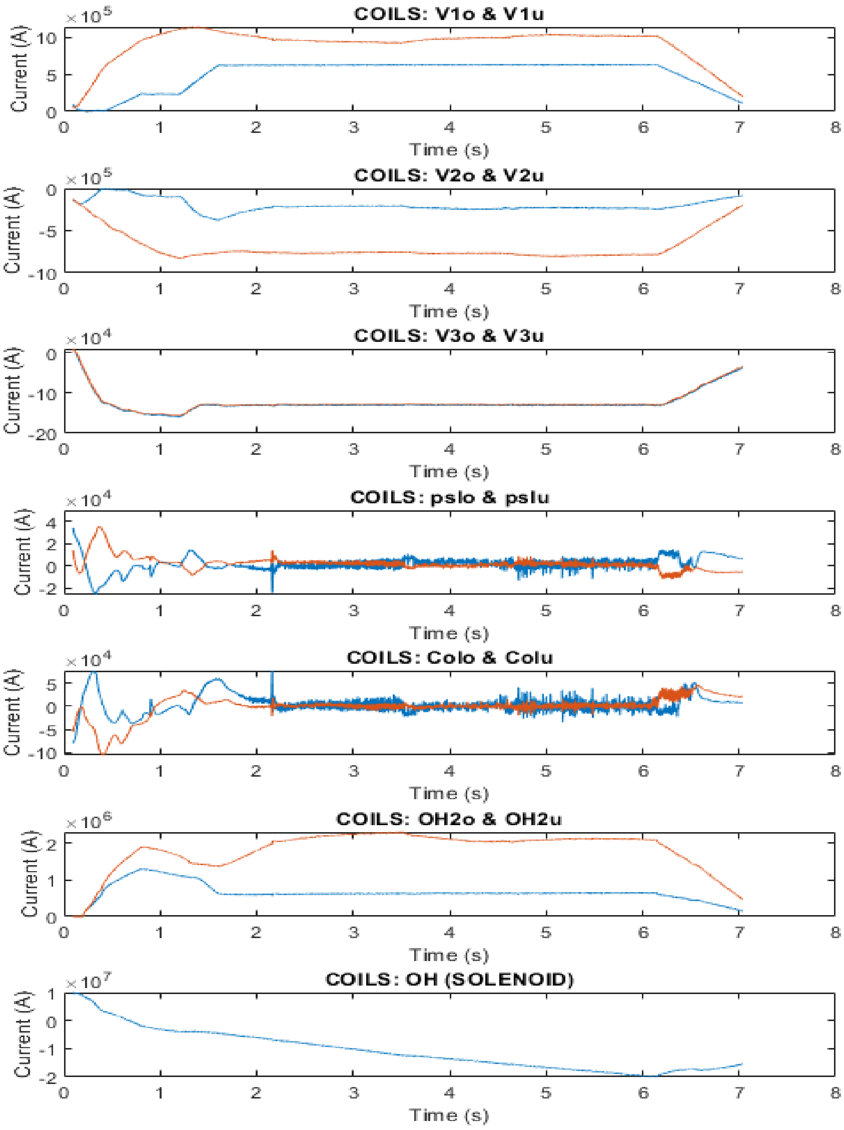

Figure 32 Current ramps values to every coil in AUG that affect to the plasma, from the discharge #39613.

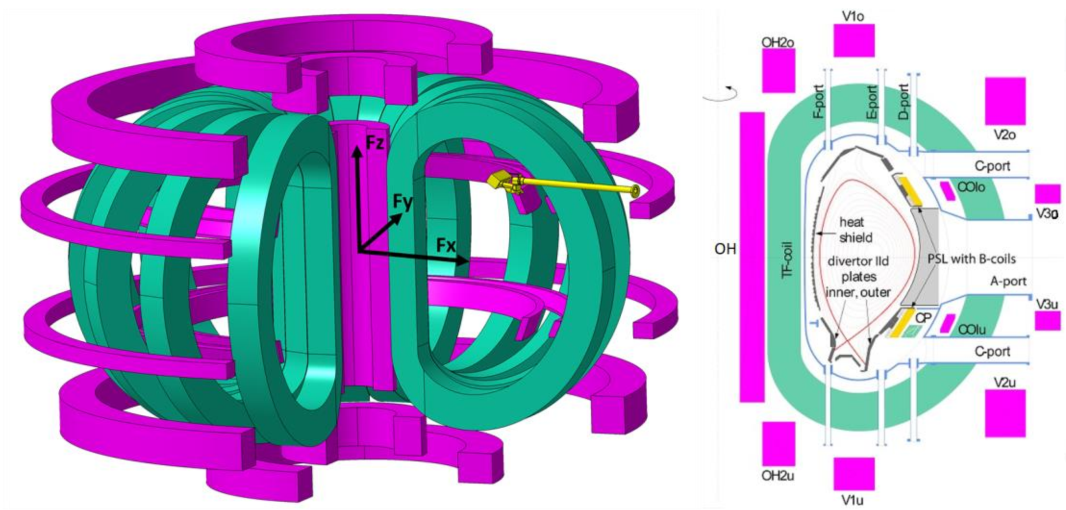

Figure 33 On the left, section of AUG coils with INPA diagnostic located in C-port with axes used in Eddy current forces. On the right, name of all of the coils as a better interpretation of the graphics. Reprinted right image [17].

In Figure 32 there are two colors due to the symmetry in the toroidal plane, the coils are similar on both sides and are represented by the same graph. The orange line represents the upper coils, and the blue lines the lower ones.

The forces (JxB) correspond to the interaction between the Eddy current that flows in the components and the magnetic field. These values are represented as Fx, Fy, Fz and these axes are shown in Figure 33.

In Figure 34 we can see the sum of all the coils that have been fed and presented in the graph of the previous image together with the INPA in its real position. The overlay graph plots the induced forces, on the INPA along the pulse, at the principal vectors of the tokamak coordinate origin, and the resultant force of all of them. The total forces represent the sum of all the forces in all the axis: $Total\ forces = Fx + Fy + Fz$.

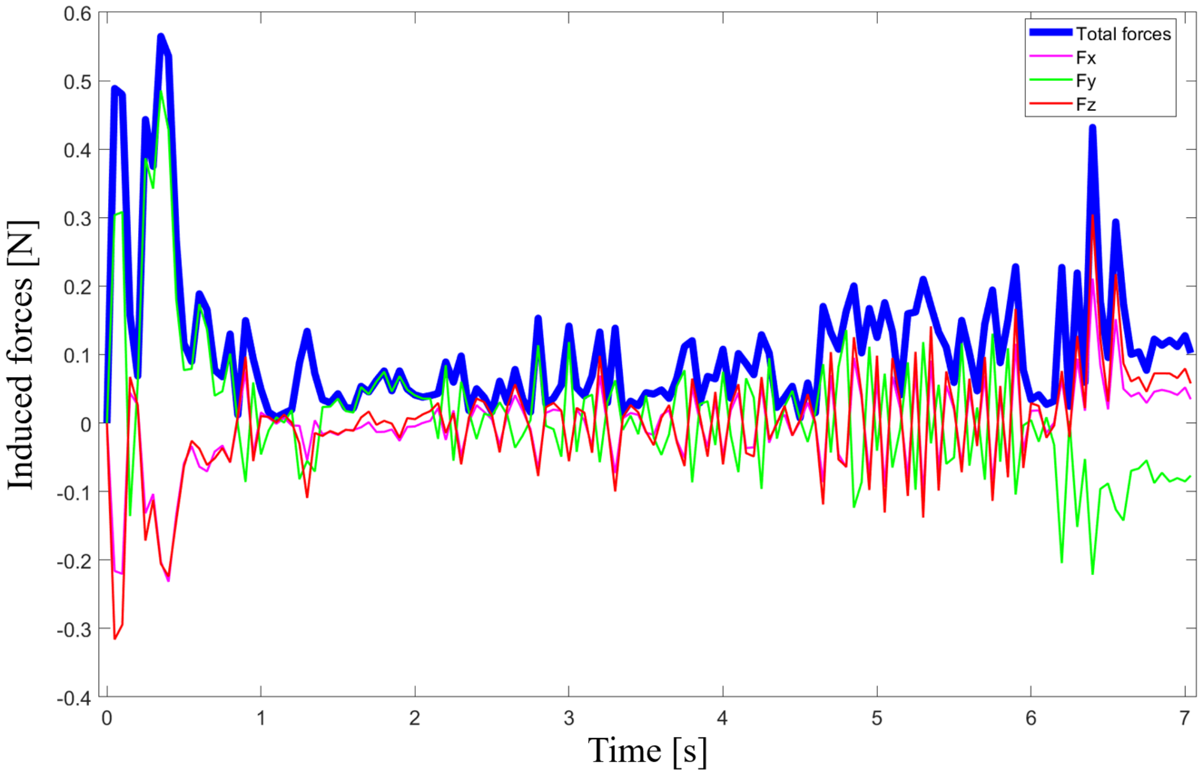

Figure 34 Induced forces [N] in INPA diagnostic**.**

The maximum value obtained is 0.6 N in $t = 0.4\ s$. Then, this maximum value is used in ANSYS Mechanical to obtain the stress produced.

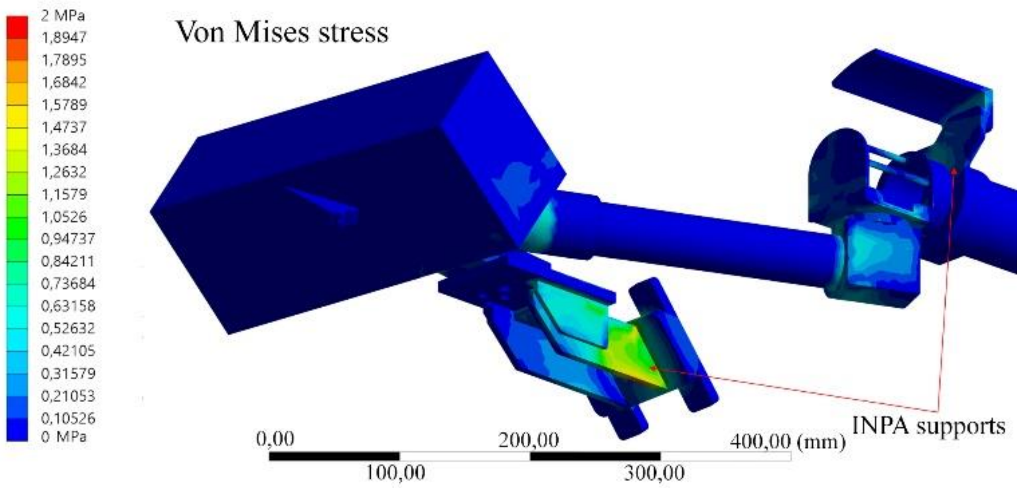

Figure 35 Maximum Von Mises stress in 0,36 second time, as the maximum value in stress in transient analysis, induced by the coil current ramps [28].

Figure 35 shows in ANSYS Mechanical, the maximum equivalent Von Mises stress collected during a pulse of 7 seconds with Eddy currents over 2 MPa. The equivalent stress concentrates in the supports, head, and periscope. Results presented can be neglected for being orders of magnitude below to the material yield strength of 290 MPa [35].

6.2.2.2 Disruption event assessment

The values of the supply current of the coils and a plasma current of 760 kA have been taken, as a representative example of pulse in ASDEX Upgrade. To evaluate a disruptive event, the plasma current needs to increase from zero to a stable value, and at some point, an event happens to drop abruptly in a short time, reducing its current to zero. This plasma time reduction is called current quench [47] and it is related to a major induction of forces to the electrically conductive components. Figure 36 shows the values used for the analysis with a current quench of 5 ms in $t = 3\ s$.

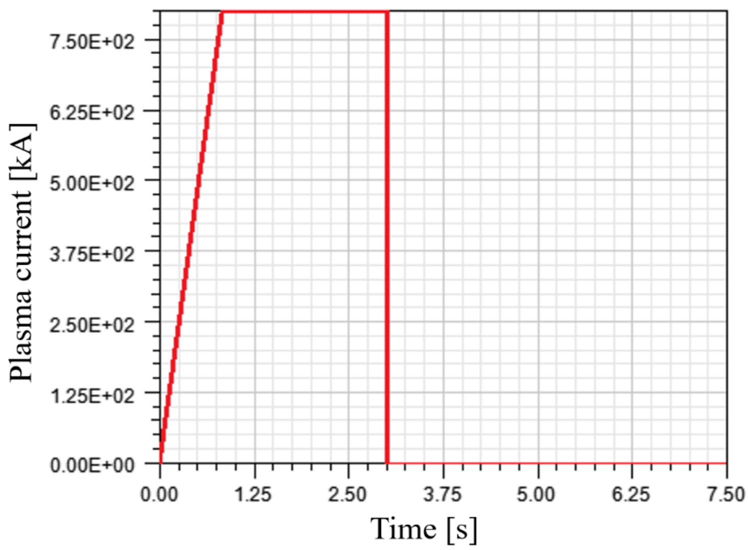

Figure 36 Simplification of plasma current during a disruptive event.

ANSYS Maxwell has been used to reproduce the same model for the Eddy current in the discharge #39613, adding a plasma current with this variation in time, $t = 3.003\ s$, to obtain the volumetric forces induces in

INPA.

We can see the forces induced in the INPA head during a disruptive event in Figure 37, with maximum values up to $4{,}2 \cdot 10^5$ N/m^3, an order of magnitude below to be considered. Forces are induced to create some torque to the connection between the head and the support. The design of this connection is done considering these charges. This connection is fixed by 2 screws M10 and 1 M16 to maintain a perfect transmission of the charges to the support.

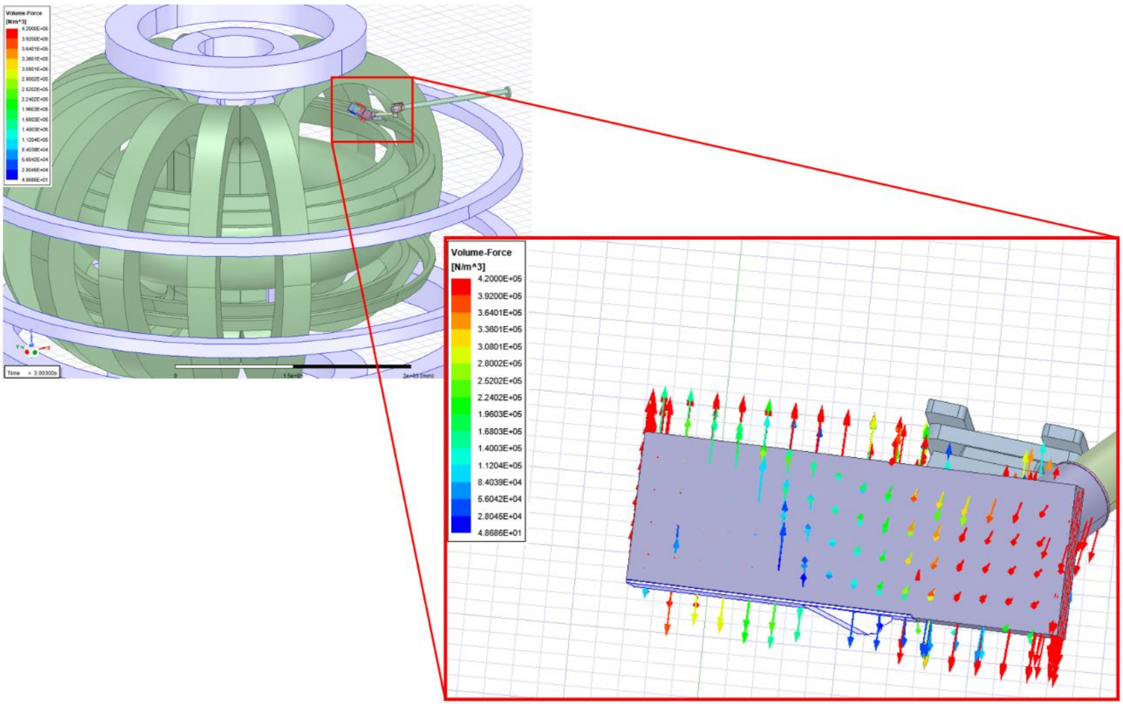

Figure 37 Volumetric forces [N/m3] induced in the INPA head during a disruptive event. INPA location between the coils in the model used in ANSYS Maxwell and a zoom in on the head.

These volumetric forces were applied in ANSYS Mechanical to obtain the stress induced. The maximum values are related to the torque produced in the connection. As can be seen, the support transmits part of the stress from the head. Considering a steel yield strength of 290 MPa and the maximum Von mises stress values that we get in Figure 38 are 8,5 MPa, we can validate the approach of the design and consider that it does not have a real impact on the system.

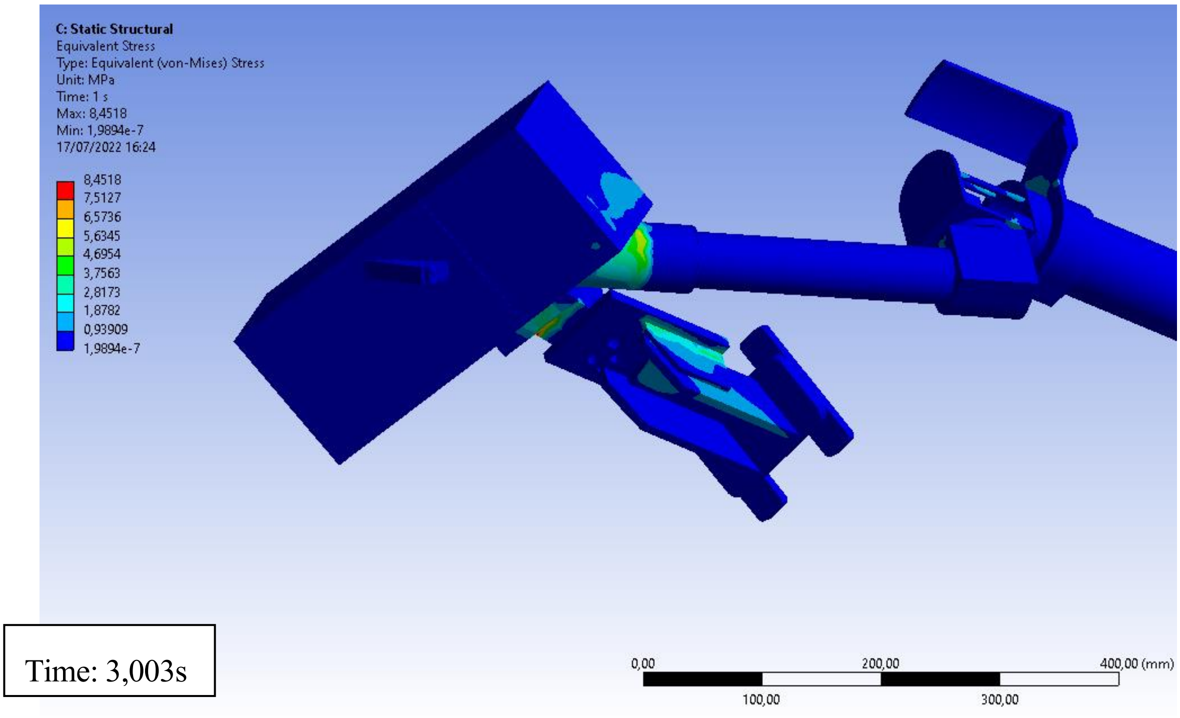

Figure 38 Maximum Von Mises stress during a disruptive event.

The structural system integrity works in a safe condition considering the low stress induced in a disruption event.

6.3 Thermal assessment

The INPA structural integrity requires overcoming the thermal charges induced during a pulse in ASDEX Upgrade.

During the previous campaign, one of the diagnostics near to the INPA, bolometer on the left in the Figure 39, left image, had its coverage of 5 mm of stainless steel melted, so we were strongly advised to evaluate the thermal loads in detail.

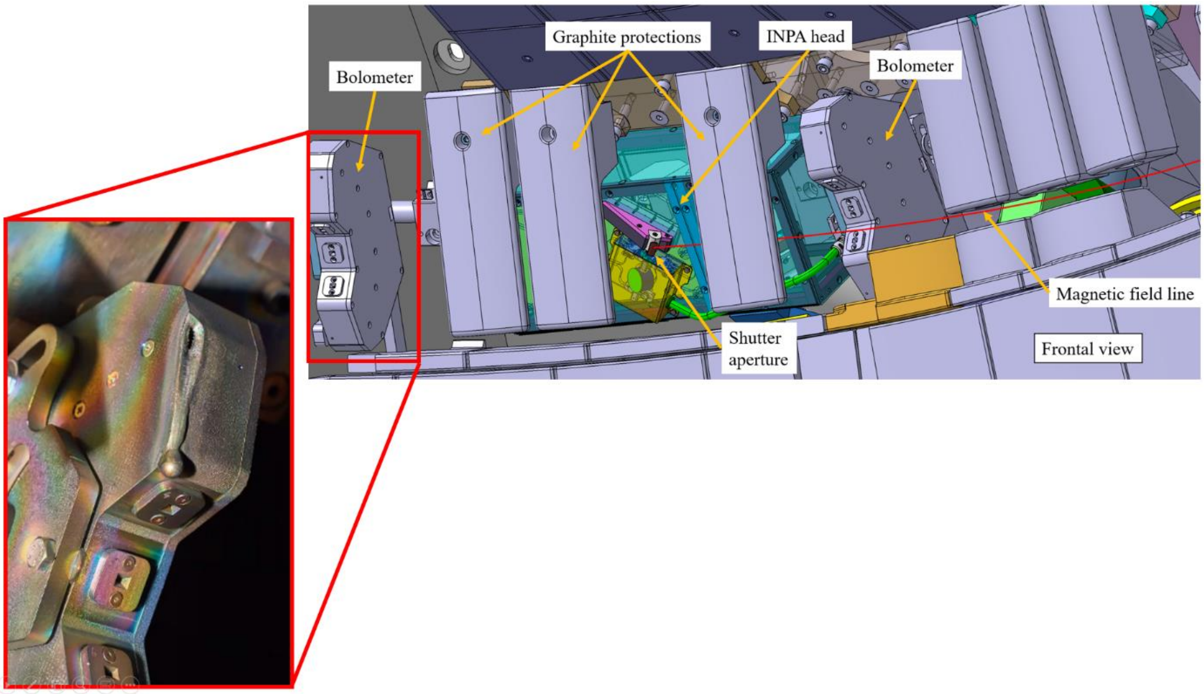

Figure 39 Position in CAD for the real bolometer with the cover melted.

To generate the heat flux induced in the head, mainly, it is studied the heat parallel to the magnetic field lines. This heat flux is the one produced by the fast particles, that follow magnetic field lines, colliding with the surface of the object to be studied. To evaluate that, the exponential λ_q model [48], [49] has been used.

Graphite protections cover the INPA front side exposed to radial heat fluxes, Figure 40, and, because of these protections and the low charge induced compared to the heat parallel to the magnetic field lines, radial heat fluxes are not contemplated on this analysis.

Figure 40 Three graphite protections protecting INPA head from the radial heat flux [28].

6.3.1 The collection length factor

The collection length factor has been used to correct the λ_q model. This factor treats the shadowing of the magnetic field lines as a non-binary state perfectly wet or shadowed surface, so then, we can used that like a continuous linear range between 0 and 1, [50].

This factor is the distance between a wet triangle, area with particle collisions, and the structure through a field line that collapses the trajectory. It gives information about how achievable is for particles to enter a determined magnetic field line via perpendicular transport.

So, if a limiter is next to the INPA head the collection factor will be close to 0. On the other hand, if the connection length is large enough (as in the case of some of the field lines reaching the pinhole cover), some particles may travel perpendicularly to this field line accounting for the parallel heat flux. Therefore, with this correction we are accounting for the impact of perpendicular transport on the parallel heat flux. For the estimation of the collection length factor a detailed mesh of the surrounding INPA structures was used.

Discharge #36524 at 2.30s, has been used as an example of heat flux dissemination for a fast-ion experiment. Using a conservative approach to explore the limits of the system [50], [51], the maximum heat flux values up to 1.99 W/mm^2 are applied to the plasma facing surfaces and elongated during an analysis of 10 seconds.

This peak heat load would not correctly represent the energy received by the detector during the whole shot, as this event only lasts for a few milliseconds. The chosen instant is a more faithful representation of the expected energy deposited on the detector during the shot.

In Figure 41, the graphic represents the parallel heat flux q_{II}, to the magnetic field lines, as a function of ρ_{pol}, where a small decrease on the distance to the plasma will not have a significant impact on the received heat flux. The blue diamonds represent the experimental divertor datapoints and the black line is the double exponential fit. The lateral position engrossed by the INPA head in ρ_{pol} is also included (red line).

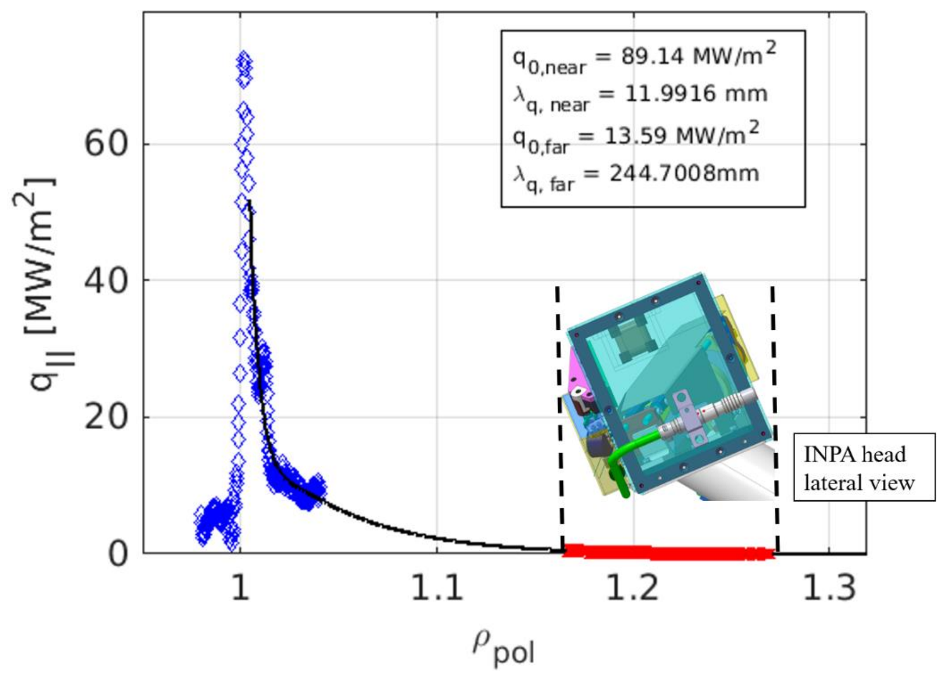

Figure 41 Represents the parallel heat flux q_{II} as a function of ρ_{pol}. The size of the INPA head is located through the red line.

The limiters, shown in Figure 42, cover the detector from the radial heat flux, while most of the parallel heat flux is stopped by the bolometers at the INPA sides. This figure has been updated to better depict the INPA surroundings. The parallel cover offered by the bolometers is not total. Field line tracing shows that some field lines may get to the pinhole. Note that these field lines are not field lines that connect the detector with the scrape-off layer, but magnetic field lines enclosed between the pinhole and other structures on the wall.

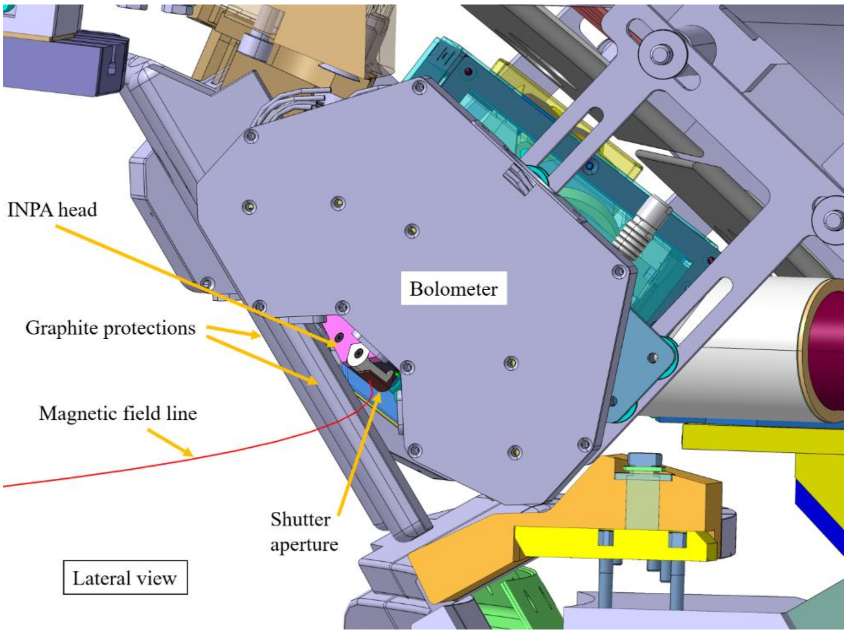

Figure 42 Lateral view of INPA diagnostic in-vessel. Magnetic field lines (red curve) avoid limiters (graphite protections) colliding with the INPA head.

6.3.2 Thermal assessment results

The maximum temperature reached along a pulse for the INPA components is presented in Figure 43. Temperature is accumulated during the discharge and the values represented are at the end of the pulse. The maximum value gets close to 1000 ºC. It is found in a small sector of a non-structural cover plate named as shutter, detailed view in Figure 43. Taken into the very conservative approach, these values are not critical compared to the material limits.

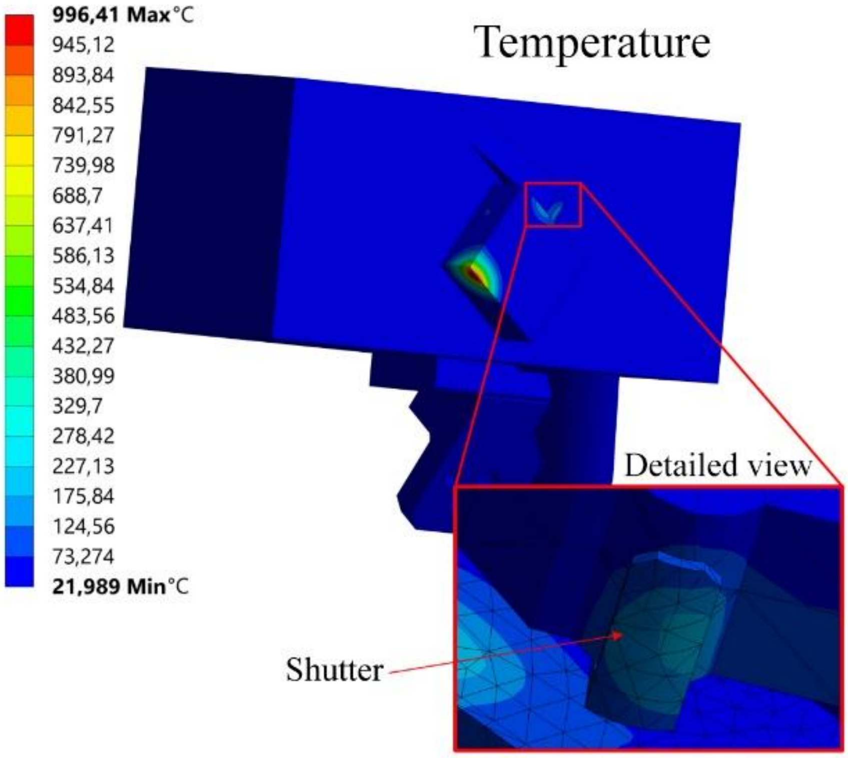

Figure 43 Maximum temperature values induced by the parallel heat flux during transient thermal assessment [28].

Detailed views in Figures 43 and 44 show the shutter plate that is a rotational system who provides to not to let enter particles in the system when INPA is not measuring. The shutter protects the carbon foil, that is 12 nm thickness, and it degrades with every particle collision, so it is essential to protect it. The shutter needs to work properly during all campaigns, letting particles in when it gets activated and close when it is necessary.

Equivalent Von Mises stress induced by the maximum temperatures is given in Figure 44. Results demonstrate the equivalent stress is low compared to the material limits. Regarding the shutter, detailed view in Figure 44, the local stress concentration appears. However, compared to the yield stress of the material, this maximum stress is not critical, and a small deformation has no impact on structural integrity or in the signal.

It should be noted that the diagnostic must work without any error during the entire campaign, since the system is in ultra-high vacuum 10^{-9} mbar and can only have maintenance work during the opening, that occurs in August. Because of that and being the shutter the only moving part, it is taken as a critical component in the study of its operation, so then, the shutter must work properly, and it cannot get any impact due to the stress induced by the heat flux. In the detailed view of Figure 43, it can be seen that temperatures and equivalent stress does not reach high values to be considered the system as a critical, so we can expect that the shutter can work properly.

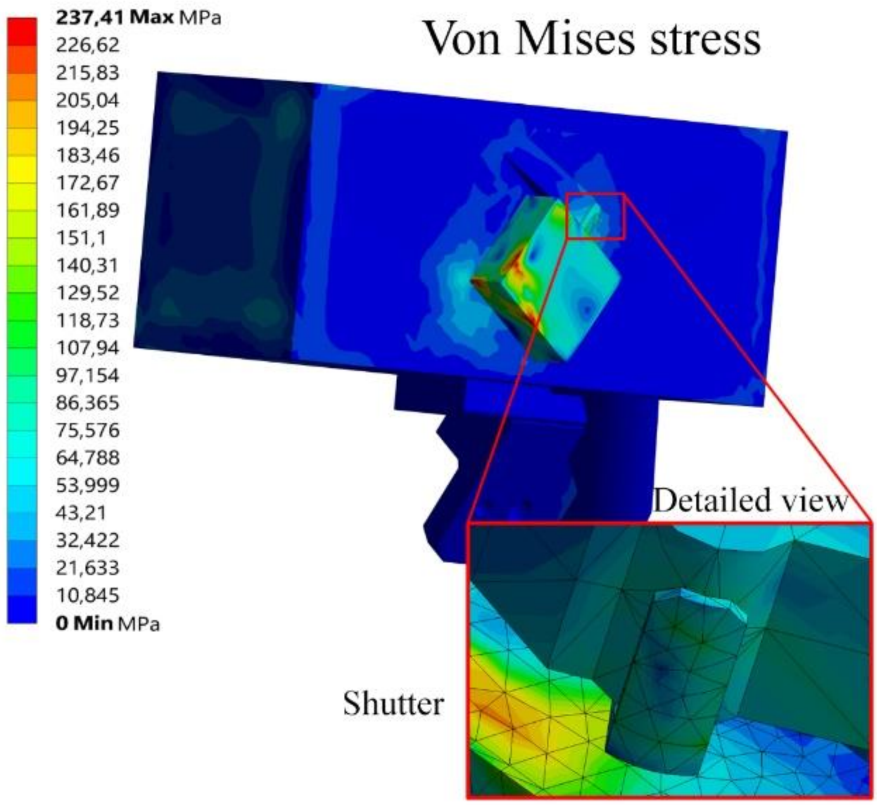

Figure 44 Maximum Von Mises stress induced by the parallel heat flux during transient thermal assessment [28].

Figure 45 represents the time evolution of the maximum stress (left) and the temperature (right). Results indicate the temperature is being increase during the plasma pulse, reaching an approximately maximum value of 1000 ºC.

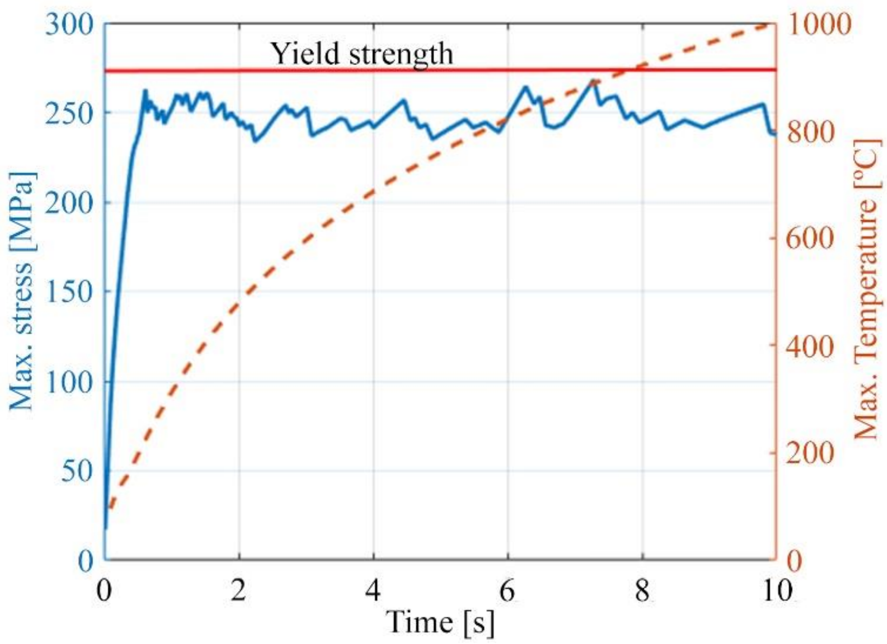

Figure 45 Maximum thermal stress and temperatures values, during the transient thermal assessment [28].

Additionally, the stress increases rapidly to the maximum value at the beginning, and it gets stabilized at around 250 MPa. This is caused by the thermal dissipations around the cover. As a result, the critical points are very small compared to the cover plate, dissipating in a faster way.

Maximum values of the temperature and stress are admissible for the system structural integrity.

7 SUMMARY AND FUTURE WORK

7.1 Summary and Conclusions

The design, analysis, assembly, and installation of the Imaging Neutral Particle Analyzer has been presented. The structural integrity of the diagnostic has been studied with Finite Element Method with ANSYS software, (Mechanical and Maxwell), validating the structural safety of the system.

The results have been summarized as follows:

- The design approach has worked without any modification time delay.
- The design of all the diagnostic components and the drawings for their manufacture have been made.
- The manufacture of all the components has been adjusted to what is demanded in the drawings without any mismatches, error tolerances.
- The assembly of the sets of components inside the reactor did not require any modifications and was carried out successfully at the indicated time.
- The optical and mechanical calibration in the laboratory and inside the reactor was done successfully with a sensitivity very close to the theoretical one.
- The design has complied with the analysis of structural integrity (EM and thermal analysis).
- INPA diagnostic is working properly, and first measurements are being published in an article [27].

7.2 Future work

During the opening of AUG that is taking place, a comparison will be made between the visual state of the diagnostic inside the vessel and the assessment results taken. The degree of correlation between the simulated and the real will be sought to verify future design procedures.

This novel diagnostic is being developed at other tokamak facilities considering the promising results obtained.

The design approach has been used as a route for design validation of future diagnostics in the research group: Plasma Science and Fusion Technology (PSFT).

8 GLOSSARY

List of symbols

E	Energy
m	Mass
c	Speed of light
Q	Gain factor
n_e	Electron density
T_e	Electron temperature
τ_E	Energy confinement time
$\vec{F}$	Force applied on the particles
q	Electric charge of the particle
$\vec{v}$	Velocity of the particle
$\vec{B}$	Magnetic field
$\overrightarrow{v_{\parallel}}$	Parallel component of velocity
$\overrightarrow{v_{\perp}}$	Perpendicular component of the velocity
ω_{C}	Lamour frequency
r_{L}	Lamour radius
p	Pitch angle
R	Major radius
z	Heigth
$Dist$	Distortion
d	Real distance between point
dr	Distorted distance
Ω	Solid angle
A	Area
r	Radius
F	F-number
R	Reduction of light
T	Light transmission
$d\vec{B}$	Variation of the magnetic
dt	Variantion of time
I_{eddy}	Eddy current
I_{input}	Feeded current
F_X	Forces induced in x axis
F_Y	Forces induced in y axis
F_Z	Forces induced in z axis
t	Time
λ_q	Exponential decay Lambda q model

List of Acronyms

CofM	Center of Momentum
Q	Gain factor
Tokamak	*Toroidal'naya kamera s magnitnymi katushkami*
UHV	Ultra High Vacuum
INPA	Imaging Neutral Particle Analyzer
AUG	ASDEX Upgrade
ASDEX	Axially Symmetric Divertor Experiment
NPA	Neutral Particle Analyzer
FILD	Fast Ions Loss Detector
CAD	Computer-Aided Design
ITER	International Thermonuclear Experiment Reactor
UHV	Ultra-high vacuum
TFC	Toroidal Field Coils
CS	Central Solenoid
PFC	Poloidal Field Coils
DEMO	DEMOnstration power plant
NBI	Neutral Beam Injection
ICRH	Ion Cyclotron Resonance Heating
ECRH	Electron Cyclotron Resonance Heating
CX	Charge-exchange
LOS	Lines Of Sights
PMT	Photomultiplier
PE	Polyethylene
DOF	Degree Of Freedom
FOV	Field Of View
EM	Electro-mechanical
FEA	Finite Element Analysis

9 REFERENCES

[1] U. E. I. Administration, "Today in energy," [Online]. Available: https://www.eia.gov/todayinenergy/detail.php?id=44095. [Accessed 13 January 2023].

[2] H. Ritchie, "What sources do we get our energy from?," [Online]. Available: https:// ourworldindata.org/ energy-mix. [Accessed 13 January 2023].

[3] E. Mearns, "Global energy forecast to 2100," [Online]. Available: https:// seekingalpha.com/ article/ 4147542-global-energy-forecast-to-2100.. [Accessed 13 January 2023].

[4] "Our World in Data," [Online]. Available: https://ourworldindata.org/grapher/years-of-fossil-fuel-reserves-left. [Accessed 13 January 2023].

[5] A. Vallet, Hydrodynamic modelling of the shock ignition scheme for inertial confinement fusion To cite this version : HAL Id : tel-01242131 DOCTEUR DE L ' UNIVERSITÉ DE BORDEAUX Modélisation hydrodynamique du schéma d ' allumage par choc pour la fusion par confineme, 2015.

[6] P. n. f. c. sections. [Online]. Available: https://scipython.com/blog/plotting-nuclear-fusion-cross-sections/. [Accessed 15 January 2023].

[7] J. A. Wesson, "Tokamaks," in *4th ed. Oxford*, Oxford University Press, 2011.

[8] G. T. COOK, "ENVIRONMENTAL LIQUID SCINTILLATION ANALYSIS," in *Handbook of Radioactivity Analysis (Second Edition)*, Elsevier Science, 2003, pp. 537-607.

[9] A. J. H. Donné, "The european roadmap towards fusion electricity," 2019. [Online]. Available: https://royalsocietypublishing.org/doi/10.1098/rsta.2017.0432. [Accessed 14 January 2023].

[10] C. P. João, Lasers, high power lasers and laser plasma interaction Plasmasurf Summer School, Instituto de Plasmas e Fusão Nuclear Instituto Superior Técnico, vol. Portugal, Lisbon, Portugal, 2018.

[11] "AIP," [Online]. Available: https://www.aip.org/fyi/2022/national-ignition-facility-achieves-long-sought-fusion-goal. [Accessed 15 January 2023].

[12] Y. Li, Thermo-Mechanical Behavior of Tungsten under Fusion-Relevant Hydrogen Plasma Loads. Phd thesis, Eindhoven University of Technology, 2021.

[13] U. S. D. o. Energy, "Project Execution Plan for the U.S. Contributions to ITER," 2017.

[14] ITER, "First Plasma: 2025," [Online]. Available: https://www.iter.org/mag/9/65. [Accessed 15 January 2023].

[15] EUROFUSION, "30 years of ASDEX Upgrade," [Online]. Available: https://www.euro-fusion.org/news/2021/march/30-years-of-asdex-upgrade/. [Accessed 15 January 2023].

[16] "Physics, Max Planck Institute For Plasma," Introduction: The ASDEX Upgrade tokamak, [Online]. Available: https://www.ipp.mpg.de/16208/einfuehrung. [Accessed 15 January 2023].

[17] A. U. fusion. [Online]. Available: https://www.ipp.mpg.de/987491/AUG_en. [Accessed 15 January 2023].

[18] X. D. Du, "Development and verification of a novel scintillator-based, imaging neutral particle analyzer in DIII-D tokamak," *Nucl. Fusion,* vol. 58, no. 8, p. 082006, 2018.

[19] J. Rueda-Rueda, "Design and simulation of an imaging neutral particle analyzer for the ASDEX upgrade tokamak," *Rev. Sci. Instrum,* vol. 92, p. 043554, 2021.

[20] M. Garcia-Munoz, «Scintillator based detector for fast-ion losses induced by magnetohydrodynamic instabilities in the ASDEX upgrade tokamak,» *Rev. Sci. Instrum,* vol. 80, p. 05350, 2009.

[21] S. S. Medley, "Contemporary instrumentation and application of charge exchange neutral particle diagnostics in magnetic fusion energy experiments," *Rev. Sci. Instrum,* vol. 79, p. 011101, 2008.

[22] N. Ida, Engineering Electromagnetics, Springer, 1999.

[23] "Field, Motion in the Presence of Magnetic," [Online]. Available: https://www.toppr.com/ask/content/concept/motion-in-the-presence-of-magnetic-field-209731/. [Accessed 15 January 2023].

[24] L. Stagner, "FIDASIM," [Online]. Available: https://d3denergetic.github.io/FIDASIM/.

[25] J. R. Rueda, Feasibility study for a new Imaging Neutral Particle Analyzer. Master thesis, University of Seville, 2018.

[26] J. Rueda-Rueda, "Design and simulation of an imaging neutral particle analyzer for the ASDEX Upgrade tokamak," *Rev. Sci. Instrum,* vol. 92, p. 43554, 2021.

[27] J. Rueda-Rueda, «First Measurements with an Imaging Neutral Particle Analyzer in the ASDEX Upgrade,» *Nucl. Fusion,* Being published.

[28] J. Garcia-Dominguez, "Imaging Neutral Particle Analyzer Engineering Design and Installation for the ASDEX Upgrade Tokamak," *IEEE TRANSACTIONS ON PLASMA SCIENCE,* vol. 50, no. 11, pp. 4138 - 4143, 2022.

[29] M. C. Jiménez-Ramos, «Characterization of scintillator materials for fast-ion loss detectors in nuclear fusion reactors,» *Nucl. Instrum. Methods Phys. Res. B, Beam Interact. Mater,* vol. 332, pp. 216-219, 2014.

[30] D. D. DiJulio, "A Polyethylene-B4C based concrete for enhanced neutron shielding at neutron research facilities," *Nuclear Instruments and Methods in Physics Research,* vol. 859, pp. 41-46, 2017.

[31] K. Magnetics, "Shielding material, What is the best material for shielding a magnet?," [Online]. Available: https://www.kjmagnetics.com/blog.asp?p=shielding-materials. [Accessed 17 January 2023].

[32] "Insulation, High-Performance PEEK Material for Wire and Cable," [Online]. Available: https://www.azom.com/equipment-details.aspx?EquipID=4445. [Accessed 17 January 2023].

[33] E. S. Blanco, «opticaldevelopment,» 2021. [En línea]. Available: http://opticaldevelopment.es/.

[34] Q. Li, «Design and alignment to off-axis reflection beam expanding and contracting optical system" Microw,» *Microw. Opt. Technol. Lett,* vol. 63, nº 10, p. 32998, 2021.

[35] C. Dasarathy, "Steels–metallurgy and applications," *Mater. Des.,* vol. 14, no. 4, p. 268, 1993.

[36] Imamagnets, "What is Lorentz's strength?," 2021. [Online]. Available: https://www.imamagnets.com/en/blog/what-is-lorentz-strength/. [Accessed 17 January 2023].

[37] E. H. Knoepfel, Magnetic Fields - A Comprehensive Theoretical Treatise for Practical Use, John Wiley & sons, 2000.

[38] J. Segado-Fernández, Mechanical Assessment of The SMART Tokamak: Vessel and Coils Supports. Master thesis, University of Malaga, 2020.

[39] J. Hromadka, «Electromagnetic model for finite element analyses of plasma disruption events used in the design phase of the COMPASS-U tokamak,» *Fusion Engineering and Design,* vol. 167, p. 112369, 2021.

[40] A. Mancini, "Mechanical and electromagnetic design of the vacuum vessel of the SMART tokamak," *Fusion Eng. Des.,* vol. 171, p. 112542, 2021.

[41] R. Ortwein, "Dynamic analysis of the forces on the COMPASS-U tokamak foundations during vertical displacement events," *AIP Conf. Proc.,* vol. 2239, no. 10.1063/5.0007822, 2020.

[42] G. Pautasso, «Disruption studies in ASDEX Upgrade in view of ITER,» *Plasma Phys. Control. Fusion,* vol. 51, p. 124056, 2009.

[43] Ansys, ANSYS Maxwell V16, 2013.

[44] G. Calabro, "Toroidal Field Ripple reduction studies for ITER and FAST," *Fusion Eng. Des.,* vol. 84, no. 2-6, pp. 522-525, 2009.

[45] J. Hromadka, "Electromagnetic model for finite element analyses of plasma disruption events used in the design phase of the COMPASS-U tokamak," *Fusion Eng. Des.,* vol. 167, p. 112369, 2021.

[46] S. Yamamoto, "Design of stabilizing plate of JT-60SA," *Fusion Eng. Des.,* vol. 168, no. 1-6, 2021.

[47] P. Heinrich, "Investigation of Alfvénic activity during the current quench in ASDEX-Upgrade," in *Vienna conference*.

[48] R. Mitteau, "Heat flux deposition on plasma-facing components using a convective model with ripple and Shafranov shift," *J. Nucl. Mater,* vol. 266–269, p. 798–803, 1999.

[49] T. Lunt, "Near- and far scrape-off layer transport studies in detached, small-ELM ASDEX upgrade discharges by means of EMC3-EIRENE," *Plasma Phys. Controlled Fusion,* vol. 62, no. 10, p. 105016, 2020.

[50] J. Hidalgo-Salaverri, "Thermo-mechanical limits of a magnetically driven fast-ion loss detector in the ASDEX upgrade tokamak," *J. Instrum.,* vol. 17, no. 2, p. 02020, 2022.

[51] J. Ayllon-Guerola, «Thermo-mechanical assessment of the JT-60 SA fast-ion loss detector,» *Fusion Eng. Des.,* vol. 167, nº 112304, 2021.

[52] U. S. Group. [Online]. Available: https://terpconnect.umd.edu/~mattland/projects/1_stellarators/. [Accessed 15 January 2023].

[53] J. Segado-Fernandez, "Analysis and Design of the Central Stack for the SMART Tokamak," *Fusion Engineering and Design,* Under publishing.